

Evolved massive stars at low metallicity

II. Red supergiant stars in the Small Magellanic Cloud[★]

Ming Yang (杨明)¹, Alceste Z. Bonanos¹, Bi-Wei Jiang (姜碧洸)², Jian Gao (高健)², Panagiotis Gavras³, Grigoris Maravelias¹, Shu Wang (王舒)⁴, Xiao-Dian Chen (陈孝钿)⁴, Frank Tramper¹, Yi Ren (任逸)², Zoi T. Spetsieri¹, and Meng-Yao Xue (薛梦瑶)⁵

¹ IAASARS, National Observatory of Athens, Vas. Pavlou and I. Metaxa, Penteli 15236, Greece
e-mail: myang@noa.gr

² Department of Astronomy, Beijing Normal University, Beijing 100875, PR China

³ Rhea Group for ESA/ESAC, Camino bajo del Castillo, s/n, Urbanizacion Villafranca del Castillo, Villanueva de la Cañada 28692, Madrid, Spain

⁴ CAS Key Laboratory of Optical Astronomy, National Astronomical Observatories, Chinese Academy of Sciences, Datun Road 20A, Beijing 100101, PR China

⁵ International Centre for Radio Astronomy Research, Curtin University, Bentley, WA 6102, Australia

Received 22 November 2019 / Accepted 20 May 2020

ABSTRACT

We present the most comprehensive red supergiant (RSG) sample for the Small Magellanic Cloud (SMC) to date, including 1239 RSG candidates. The initial sample was derived based on a source catalog for the SMC with conservative ranking. Additional spectroscopic RSGs were retrieved from the literature, and RSG candidates were selected based on the inspection of *Gaia* and 2MASS color-magnitude diagrams (CMDs). We estimate that there are in total ~1800 or more RSGs in the SMC. We purify the sample by studying the infrared CMDs and the variability of the objects, though there is still an ambiguity between asymptotic giant branch stars (AGBs) and RSGs at the red end of our sample. One heavily obscured target was identified based on multiple near-IR and mid-IR (MIR) CMDs. The investigation of color-color diagrams shows that there are fewer RSGs candidates (~4%) showing PAH emission features compared to the Milky Way and LMC (~15%). The MIR variability of RSG sample increases with luminosity. We separate the RSG sample into two subsamples (risky and safe), and identify one M5e AGB star in the risky subsample based on simultaneous inspection of variabilities, luminosities, and colors. The degeneracy of mass loss rate (MLR), variability, and luminosity of the RSG sample is discussed, indicating that most of the targets with high variability are also the bright ones with high MLR. Some targets show excessive dust emission, which may be related to previous episodic mass loss events. We also roughly estimate the total gas and dust budget produced by entire RSG population as $\sim 1.9_{-1.1}^{+2.4} \times 10^{-6} M_{\odot} \text{ yr}^{-1}$ in the most conservative case, according to the derived MLR from IRAC1–IRAC4 color. Based on the MIST models, we derive a linear relation between T_{eff} and observed $J - K_s$ color with reddening correction for the RSG sample. By using a constant bolometric correction and this relation, the Geneva evolutionary model is compared with our RSG sample, showing a good agreement and a lower initial mass limit of $\sim 7 M_{\odot}$ for the RSG population. Finally, we compare the RSG sample in the SMC and the LMC. Despite the incompleteness of LMC sample in the faint end, the result indicates that the LMC sample always shows redder color (except for the IRAC1–IRAC2 and WISE1–WISE2 colors due to CO absorption) and higher variability than the SMC sample, which is likely due to a positive relation between MLR, variability and the metallicity.

Key words. infrared: stars – Magellanic Clouds – stars: late-type – stars: massive – stars: mass-loss – stars: variables: general

1. Introduction

Red supergiant stars (RSGs) are moderately massive stars ($\sim 8\text{--}30 M_{\odot}$) in the helium-burning evolutionary phase, and are located in the upper right (cool and luminous) region of the Hertzsprung-Russell (H-R) diagram. They are the result of core hydrogen exhausted main-sequence stars, which streak across the top of the H-R diagram. As a unique class of the massive star population, their young ages ($\sim 8\text{--}20$ Myr), low effective temperature ($T_{\text{eff}} \sim 3500\text{--}4500$ K), high luminosities ($\sim 4000\text{--}400\,000 L_{\odot}$), and large radii ($\sim 100\text{--}1000 R_{\odot}$) represent

a critical extremity of stellar evolution (Humphreys & Davidson 1979; Levesque et al. 2005; Ekström et al. 2013; Massey 2013; Davies et al. 2017).

In general, RSGs are considered to have two destinies, depending on the initial mass, chemical composition, and more importantly, the mass loss rate (MLR). Some of them may stay in the RSG stage and eventually explode as hydrogen-rich Type II-P supernovae (SN). The others may evolve backwards to the blue end of the H-R diagram and spend short periods of time as yellow supergiant stars (YSGs), blue supergiant stars (BSGs), or Wolf-Rayet stars (WRs) before the final SN explosion (Smartt et al. 2009; Humphreys 2010; Ekström et al. 2012; Meynet et al. 2015; Davies & Beasor 2018). In any case, the strong mass loss during the RSG phase may largely influence the ultimate fate of the RSGs, and significantly

[★] Full Table 2 is only available at the CDS via anonymous ftp to cdsarc.u-strasbg.fr (130.79.128.5) or via <http://cdsarc.u-strasbg.fr/viz-bin/cat/J/A+A/639/A116>

contribute to the dust content and chemical enrichment of young stellar populations. Specially, RSGs may be one of the main contributors to dust production in young galaxies at high redshift, where the metallicity is much lower than the local Universe and the potential dust producer of asymptotic giant branch stars (AGBs) are not yet evolved (Massey et al. 2005; Levesque 2010). However, the major physical mechanisms (e.g., episodic mass loss, stellar winds, pulsation, convection, luminosity, metallicity, binarity) that dominate the mass loss of RSGs are still unclear (MacGregor & Stencel 1992; Harper et al. 2001; Yoon & Cantiello 2010; Maun & Josselin 2011; Beasor & Davies 2016).

To better understand the nature of the RSGs, it is crucial to build a representative sample of RSGs covering wide ranges of both metallicities and luminosities. For the low-metallicity environments, there are two excellent examples in the local Universe, the Large and Small Magellanic Cloud (LMC and SMC; about one-half and one-fifth of the metallicity of the Milky Way, respectively; Russell & Dopita 1992; Rolleston et al. 2002; Keller & Wood 2006; Dobbie et al. 2014; D’Onghia & Fox 2016). Due to their proximity, each individual star in the MCs can be resolved, which results in numerous studies for the massive stars in the past half century (Feast et al. 1980; Barba et al. 1995; Massey & Olsen 2003; Evans & Howarth 2008; Neugent et al. 2010; Bouret et al. 2013; Kourniotis et al. 2014; Hainich et al. 2015; Castro et al. 2018). However, one of the obstacles to studying massive stars in the MCs is the foreground contamination; for example, the low-mass red dwarfs in the Milky Way appear to have similar brightness to the RSGs in the MCs, and the contamination is even worse for the low-luminosity RSGs. As a result of the contamination and also the efficiency of the observation, previous studies only focused on the bright end of RSG population. Fortunately, this problem can be largely solved by utilizing the *Gaia* Data Release 2 (DR2) (Gaia Collaboration 2016, 2018), for which we have built a multiwavelength source catalog and identified three evolved massive star populations (BSGs, YSGs, and RSGs) in the SMC (Yang et al. 2019).

In this paper we present the analysis of the most comprehensive RSG sample in the SMC to date. The sample selection and data analysis are presented in Sects. 2 and 3, respectively. The discussion is described in Sect. 4. The summary is given in Sect. 5.

2. Sample selection

The main sample of RSG candidates in the SMC was derived from a source catalog for the SMC (Yang et al. 2019). We only briefly describe here the dataset and more details can be found in the original paper. The SMC source catalog is a clean magnitude-limited (IRAC1 or WISE1 ≤ 15.0 mag; Werner et al. 2004; Wright et al. 2010) multiwavelength source catalog with 45 466 targets in total. It contains data in 50 different bands including 21 optical and 29 infrared (IR) bands, ranging from ultraviolet to far-IR. Additionally, radial velocities and spectral classifications are collected from the literature, and the IR and optical variability statistics are derived from different datasets. The catalog was essentially built upon a 1'' crossmatching and a 3'' deblending between the *Spitzer* Enhanced Imaging Products (SEIP) source list and *Gaia* DR2 photometric data. We removed the foreground contamination by further constraining the proper motions and parallaxes from *Gaia* DR2. By using the evolutionary tracks and synthetic photometry from Modules for Experiments in Stellar Astrophysics (MESA; Paxton et al.

2011, 2013, 2015, 2018) Isochrones & Stellar Tracks (MIST¹; Choi et al. 2016; Dotter 2016) and also the theoretical $J - K_S$ color cuts (Cioni et al. 2006a; Boyer et al. 2011), we identified three evolved massive star populations of BSGs, YSGs, and RSGs in the SMC from five different color-magnitude diagrams (CMDs). There are 1405 RSG, 217 YSG, and 1369 BSG candidates. We ranked the candidates based on the intersection of different CMDs, where Rank 0 was given to a target identified as the same type of evolved massive star in all five CMDs by the MIST models and Rank 5 indicated the additional RSG candidates identified by the theoretical $J - K_S$ color cuts but not recovered by the MIST models.

The main RSG sample contains 1405 candidates from the SMC source catalog. However, targets with Rank 4 and 5 are selected only in one CMD by either the MIST models or the theoretical $J - K_S$ color cuts, and many of them reach down close to the tip of the red giant branch (TRGB) and AGB population (see also Figs. 13 and 14 of Yang et al. 2019). To be on the safe side we adopted only targets with ranks from 0 to 3 (targets identified in at least two CMDs) as our initial sample, which resulted in 1107 targets. Due to the photometric quality cuts and uncertainties of the *Spitzer* and *Gaia* data, the strict constraints on the astrometric solution, and the deblending applied during the construction of the source catalog, some of the spectroscopically confirmed RSGs were also rejected. In order to make the sample as complete as possible, we retrieved and added all known spectroscopic RSGs in both optical and mid-infrared (MIR) bands from Simbad (Wenger et al. 2000) and data taken by *Spitzer* Infrared Spectrograph (IRS; Houck et al. 2004), respectively. From Simbad, we selected 322 RSGs with $RV \geq 90$ km s⁻¹, spectral type later than G0, and luminosity class brighter than II by using criteria query (Levesque 2013; González-Fernández et al. 2015), for which 192 targets were matched with our initial sample within 1''. Additionally, a crossmatching with the main RSG sample of 1405 candidates indicated that three Rank 4 candidates were also matched within 1''. Surprisingly, there are two spectroscopic RSGs matched with the source catalog within 1'', but not selected as the RSG candidates by either the MIST models or the theoretical $J - K_S$ color cuts. Visual inspection of *Gaia* and 2MASS (Two Micron All Sky Survey; Skrutskie et al. 2006) CMDs (shown below) indicated that these two targets were slightly off the blue and red boundaries of the RSG region, respectively, which was likely due to the intrinsic variability of the RSGs (Kiss et al. 2006; Yang & Jiang 2011; Ren et al. 2019). Consequently, in total, there are 127 unselected spectroscopic RSGs from Simbad. For data taken by *Spitzer*/IRS, there were 22 RSGs from Ruffe et al. (2015), who classified 209 point sources observed by *Spitzer*/IRS using a decision tree method, based on IR spectral features, continuum and spectral energy distribution shape, bolometric luminosity, cluster membership, and variability information (all the targets from Kraemer et al. 2017 were also included). Of these 22 RSGs, 16 of them were matched with our initial sample within 1'', and 4 of them were matched with the previous unselected Simbad RSGs within 1''. Thus, there are only two unselected spectroscopic RSGs from *Spitzer*/IRS. In total, there are additional 129 spectroscopic RSGs from both Simbad and *Spitzer*/IRS, for which we give them Rank -1.

Since the additional crossmatching between Simbad and the main RSG sample indicated that three Rank 4 candidates were also spectroscopic RSGs, it occurred to us that there might be more RSGs among the Rank 4 candidates. However, due to lack of spectroscopic data, we are only able to identify RSG

¹ <http://waps.cfa.harvard.edu/MIST/>

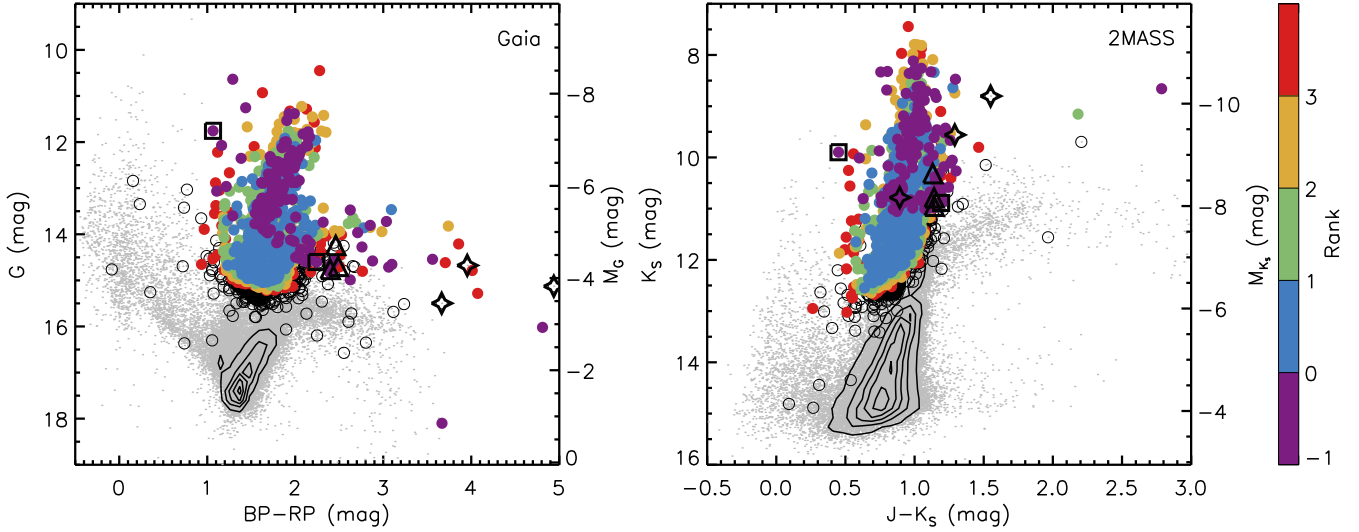


Fig. 1. Color-magnitude diagrams of *Gaia* and 2MASS datasets. Targets from the SMC source catalog are shown as gray dots. The valid RSG candidates are shown as solid circles and are color-coded ranging from Rank -1 to 3 . Three Rank 4 spectroscopic RSGs are shown as open triangles, while the other three Rank 4 CMD RSG candidates are shown as open stars. Two unselected spectroscopic RSGs are shown as open squares. The rest of Rank 4 and 5 targets from the main RSG sample are shown as open circles. Black contours represent the number density of the SMC source catalog. See text for details.

candidates with extreme red colors and high luminosities because there are probably only two kinds of candidates in the luminous red end: RSGs and super-AGBs (stars in the mass range of $\sim 7\text{--}10 M_{\odot}$ that represent a transition to the more massive supergiant stars and are characterized by degenerate off-center carbon ignition analogous to the earlier helium flash; Herwig 2005; Siess 2006; Groenewegen et al. 2009; Doherty et al. 2017). We also expect that super-AGBs could be rejected by using several methods as shown in Yang et al. (2018). As a result, another three Rank 4 CMD candidates were identified by simultaneous visual inspection of *Gaia* and 2MASS CMDs (shown below), for which they were all brighter than the AGBs branch in both CMDs, except one in the 2MASS CMD. However, the exceptional target is located well inside the RSGs region, even though it has similar luminosity compared to the bright end of AGBs population.

In total, we have 1242 RSG candidates in our valid RSG sample, with 1107 targets ranked from 0 to 3 , 129 target ranked -1 , and 6 targets ranked 4 . There are 327 unique spectroscopic RSGs from Simbad and *Spitzer*/IRS after removing the duplications. The same format of datasets as the SMC source catalog were retrieved for the newly added RSG candidates (see Table 3 of Yang et al. 2019 regarding the form and content of the table). Figure 1 shows the CMDs of *Gaia* and 2MASS datasets, where the valid RSG sample is overplotted on the SMC source catalog. We use a canonical value of 18.95 ± 0.07 as the distance modulus of the SMC (Graczyk et al. 2014; Scowcroft et al. 2016). However, it is worthwhile mentioning that SMC also has a 3D structure, with a full depth of ~ 0.4 mag (Jacyszyn-Dobrzniecka et al. 2016; Muraveva et al. 2018), which is discussed later. It appears that the valid RSG sample occupies the most luminous red regions in both CMDs. The extended branch towards the red end (presumably the dusty RSGs) in the *Gaia* CMD is distinctly brighter than the AGBs population. The sample extends to $M_G \approx -4.0$ mag and $M_{K_S} \approx -6.0$ mag, respectively. Figure 2 shows the spatial distribution of the valid RSG sample overlapped on the cropped *Spitzer* $8.0\mu\text{m}$ mosaic image, for which the stretching of the targets towards the Magellanic Bridge (MB) due to the interaction of the LMC and SMC is obviously seen.

We further purified the sample by studying the infrared CMDs and the variability of the objects as described in the next section.

Moreover, we would like to emphasize that even though our sample size is almost one order of magnitude larger than a decade ago, it is not yet fully complete due to the limitations mentioned above. A quick comparison between our sample and a new spectroscopic RSG sample in the SMC (Philip Massey, priv. comm.) indicates that our main RSG sample (1405 targets with Rank 0 to 5) and valid RSG sample (1242 targets with Rank -1 to 4) may reach to about 80% and 90% completeness down to $K_S \leq 11.0$ mag, respectively. In that sense, based on the $\sim 80\%$ completeness of the main sample (there is almost no spectroscopic RSG fainter than $K_S = 11.0$ mag), we expect a total of ~ 1800 or more RSGs in the SMC.

3. Data analysis

3.1. 2MASS color-magnitude diagrams

A robust sample is the basis for our study of the RSGs population in the SMC. Since the emission peak of RSGs is close to the near-infrared (NIR) bands due to the low T_{eff} , the IR data have lower variability and are less affected by extinction than the optical data (Chiosi & Maeder 1986; van Loon et al. 1999; Maun & Josselin 2011), the NIR and MIR CMDs are used as the first approach to purify and evaluate the RSGs sample. First of all, we considered the 2MASS bands as the primary standard. It is not only because of the reasons mentioned above, but also because the 2MASS bands are still mainly dominated by the stellar radiation instead of the dust emission, and both the MIST models and the theoretical $J - K_S$ color cuts are available in 2MASS bands.

The left panel of Fig. 3 shows the K_S versus $J - K_S$ diagram of the SMC source catalog (gray dots) overlapped with 1242 RSG candidates (red solid circles). The foreground extinction of the SMC was not taken into account since it was very low in the 2MASS bands ($A_J \approx 0.03$ and $A_{K_S} \approx 0.01$ mag), and comparable to the observational uncertainty, if $E(B - V) \sim 0.06$ mag with the Galactic average value of $R_V = 3.1$ was adopted

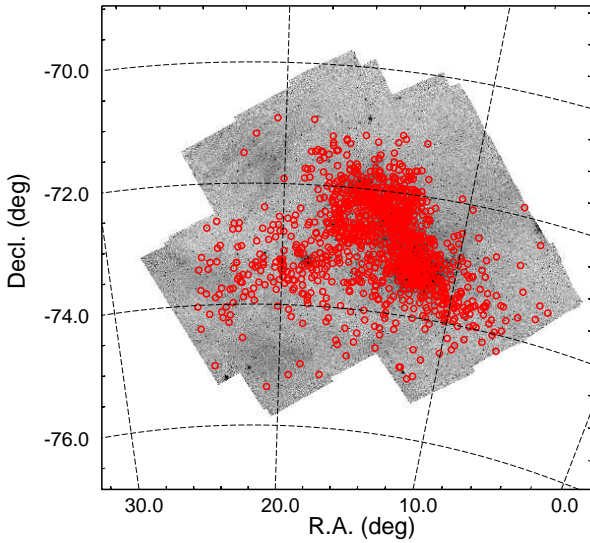


Fig. 2. Spatial distribution of 1242 RSG candidates overlapped on the cropped *Spitzer* $8.0\ \mu\text{m}$ mosaic image (north up and east to the left). Part of the targets are stretching towards the MB (in the direction of southeast) due to the interaction between the LMC and the SMC.

(Bessell et al. 1991; Gao et al. 2013). Considering $A_{K_S}/A_V \sim 0.1$ and the universal IR extinction law (Rieke & Lebofsky 1985), a reddening vector of $A_{K_S} = 0.1$ mag is shown for reference by using a precise interstellar dust extinction law from Wang & Chen (2019) (it may not show in some diagrams below since it is too small to see). We note that these extinction coefficients are only a good approximation due to the large difference in the metallicity between the SMC and the Milky Way. The regions of different evolved massive star populations (BSGs, YSGs, and RSGs) defined by the MIST models are shown as dashed lines (the boundaries between RSGs, YSGs, and BSGs are simply defined at $T_{\text{eff}} = 5000$ and 7500 K, respectively; see also Figs. 13 and 14 of Yang et al. 2019). The regions of oxygen-rich AGBs (O-AGBs; $K_S < K_S\text{-TRGB}$ (≈ 12.7 mag, dotted line; Cioni et al. 2000) and $K1 < J - K_S < K2$), carbon-rich AGBs (C-AGBs; $K_S < K_S\text{-TRGB}$ and $K2 < J - K_S < 2.1$ mag), extreme-AGBs (x-AGBs; $J - K_S > 2.1$ mag), and RSGs (K_R ; $\Delta(J - K_S) = 0.25$ mag from the O-AGBs) defined by the theoretical $J - K_S$ color cuts are shown as solid lines (all AGBs are brighter than the K0 line except x-AGBs; the distance and 0.05 mag for the metallicity between the LMC and the SMC are corrected; Cioni et al. 2006b; see more details in Sect. 3 of Boyer et al. 2011 and Sect. 4 of Yang et al. 2019).

At the bright end it can be seen that all the spectroscopic RSGs are brighter than $K_S \approx 11.0$ mag and only represent about 25% of the whole population. It is not even fully representative of the bright population since there are around 600 targets with $K_S \lesssim 11.0$ mag. This prevents us from constraining the RSGs population solely based on the incomplete sample of spectroscopic RSGs, until the next generation of large-scale spectroscopic data are obtained (e.g., 4MOST, MOONS; Cirasuolo et al. 2012; de Jong et al. 2012). We also would like to emphasize that, due to the strict constraints applied to our source catalog and also the limitations of different catalogs (e.g., saturation limits, photometric quality cuts, sky coverage and so on), there may still be a very small chance that we miss a few targets at the very bright end (e.g., $K_S \sim 8.0$ mag; most likely due to the saturation problem of *Spitzer*). However, since a comparison between our valid sample and a quick

crossmatching of the 2MASS point source catalog (which is less constrained and also shallower than our source catalog) and *Gaia* DR2 with relaxed criteria indicated that the bright ends of two samples were identical, we concluded that we did not lose any of the brightest RSGs.

At the faint end, we excluded targets fainter than both the $K_S\text{-TRGB}$ ($K_S \approx 12.7$ mag) and IRAC1-TRGB (IRAC1 ≈ 12.6 mag; Boyer et al. 2011), to eliminate possible contamination from the red giant branch stars (RGBs), since our sample reached down to the TRGB. Two targets were identified, which resulted in a reduced sample of 1240 RSG candidates. By checking the TRGBs in both K_S and IRAC1 bands, we ensured that the obscured targets were not excluded (Boyer et al. 2011). However, it should be noted that as we do not include the majority of RSG candidates with Rank 4 or 5, there is still a chance that some of them may be true RSGs. Furthermore, even if we constrain our sample to be brighter than the TRGB, as shown in Fig. 15 of Yang et al. (2019), there are still some targets from the RSG branch that extend towards fainter magnitude. In particular, there are hundreds of targets clumping at the region between RSGs, RGBs, AGBs, and red clump stars (RCs). Currently, the nature of these fainter targets is unknown, but could be a mixture of different populations including very faint RSGs.

For the blue end of the $J - K_S$ color, we expect there to be overlapping between the RSGs and YSGs, which is due to three factors. First, there is no clear boundary between RSGs and YSGs. Second, some RSGs can change spectral type from early-K to late-G due to variability. Third, the average spectral type of RSGs shifts towards earlier types at lower metallicities (Levesque et al. 2006; Massey et al. 2007; González-Fernández et al. 2015; Dorda et al. 2016).

For the red end of the $J - K_S$ color, as described in Sect. 4 of Yang et al. (2019), there was a discrepancy between the MIST models and the theoretical $J - K_S$ color cuts, where a significant number of RSGs candidates (206 targets) selected by the MIST models were located within the O-AGBs region defined by the theoretical color cuts. Among them, $\sim 23\%$ (47 targets) are spectroscopic RSGs. This poses a real dilemma for defining the RSG population. On the one hand, considering that the majority of the spectroscopic RSGs are brighter than $K_S \approx 11.0$ mag, the ratio of the spectroscopic RSGs is as high as $\sim 43\%$ (46/106; with $K_S \leq 11.0$ mag) for the RSG candidates in the O-AGBs region. Moreover, the right panel of Fig. 3 shows the zoomed-out region of $8.0 \leq K_S \leq 12.0$ mag and $0.8 \leq J - K_S \leq 1.5$ mag, where the distribution of the optical spectroscopic RSGs at the red end follows almost exactly the MIST tracks, indicating that the MIST models may be correct to a certain extent since there is no spectroscopic RSG in the fainter magnitude up to now. On the other hand, many spectroscopic classifications are based on line ratios or morphological classifications (Dorda et al. 2018), which are a continuum from AGBs to RSGs, and both the RSGs and AGBs show spectral variability (Bessell et al. 1996; Dorda et al. 2016). This probably means that spectroscopic identification may not be a golden standard, as the difference between AGBs and RSGs is not always evident when looking at a spectrum, especially at the overlapping region of the CMD.

For further analysis, the left panel of Fig. 4 shows the same diagram of K_S versus $J - K_S$ with variable classifications (Soszyński et al. 2011, 2015, 2018; Pawlak et al. 2016) from the Optical Gravitational Lensing Experiment (OGLE; Udalski et al. 1992, 2008, 2015; Szymanski 2005), and are matched with our source catalog and RSG sample within $1''$ (the numbers and classifications are listed in Table 1). Initially, it appears that many carbon-rich OGLE small amplitude red giants

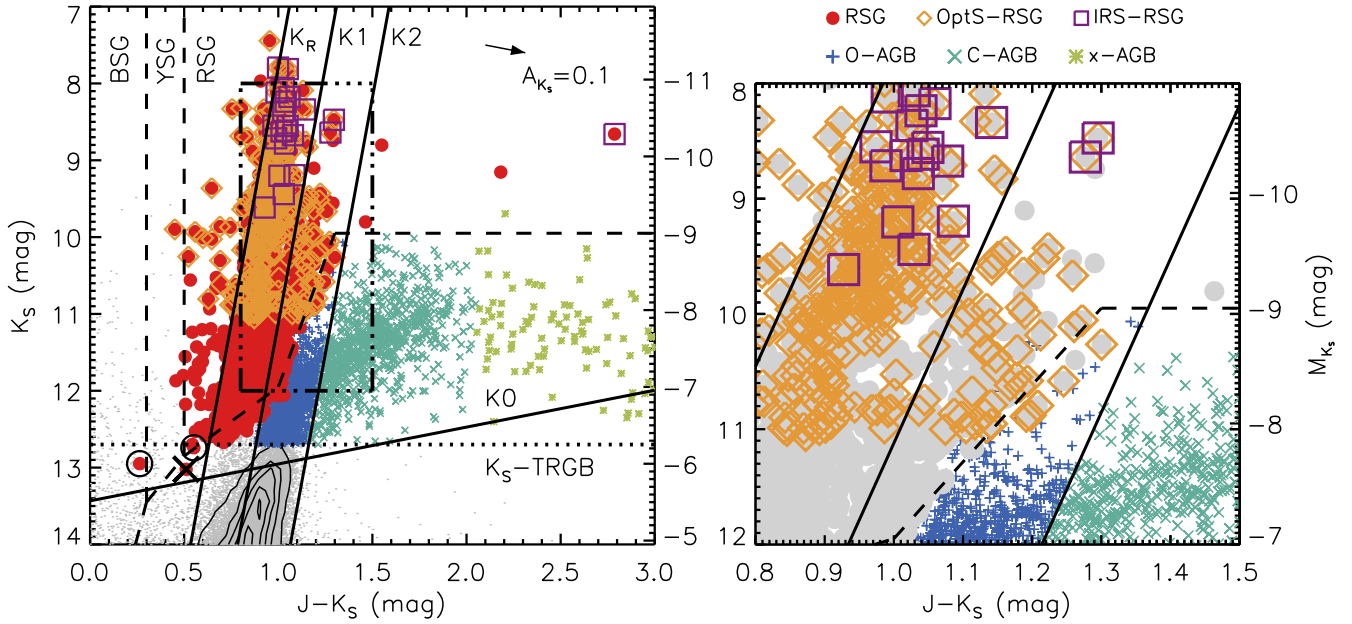


Fig. 3. K_S vs. $J - K_S$ CMDs showing RSG and AGB candidates. *Left panel:* targets from the SMC source catalog are shown as gray dots with contours indicating the number density (same below), while the 1242 RSGs candidates are shown as solid circles. The O-AGB (pluses), C-AGB (crosses), x-AGB (asterisks), and RSG populations defined by theoretical $J - K_S$ color cuts are separated by K0, K1, K2, and K_R lines (solid lines), respectively (same below). The regions of BSG, YSG, and RSG populations defined by the MIST models are separated by the dashed lines. The optical and MIR spectroscopic RSGs are shown as open diamonds and open squares, respectively, and only represent about 25% of the whole RSG population. A reddening vector of $A_{K_S} = 0.1$ mag is shown as a reference. Two targets both fainter than the K_S -TRGB ($K_S \approx 12.7$ mag; dotted line) and IRAC1-TRGB (IRAC1 ≈ 12.6 mag) are excluded from the RSG sample, and are marked as big open circles. One heavily obscured target is shown as big cross (same below). The zoomed-out region is indicated by dash-dotted lines. *Right panel:* zoomed-out region of $8.0 \leq K_S \leq 12.0$ mag and $0.8 \leq J - K_S \leq 1.5$ mag, where the distribution of the optical spectroscopic RSGs at the red end follows almost exactly the MIST tracks. See text for details.

(C-OSARGs) are located within the O-AGBs region between the K1 line and the red boundary of the MIST models and overlap with our RSG sample. Meanwhile, the same zoomed-out region (right panel of Fig. 4) indicates that 24 C-OSARGs, 7 oxygen-rich semiregular variables (O-SRVs) and 3 oxygen-rich Miras (O-Miras) are optical spectroscopic RSGs. When considering targets with $K_S \leq 11.0$ mag, the ratio of spectroscopic RSGs for C-OSARGs, O-SRVs, and O-Miras is about one-third ($\sim 34\%$; 22/64), one-half ($\sim 54\%$; 7/13), and one-fourth (25%; 3/12), respectively. Still, similar to the spectral conundrum, the variable classification also has the same problem. It was mainly done based on the light curve (LC) morphology, position of a star in the period-luminosity, color-magnitude, and period-amplitude diagrams (Soszyński et al. 2011). This process was complex, due to the complicated nature of the LCs, which often showed multiperiodicity, irregular variations, changes of the mean magnitudes, or modulations of periods, phases, and amplitudes (Soszyński et al. 2009). In that sense, there is again a continuum with similarity and overlapping from OSARGs to SRVs to Miras, which can also be seen from the two panels of Fig. 4. It is possible that some medium- or low-luminosity RSGs, which are supposedly SRVs, are misclassified as OSARGs or Miras, but vice versa. The LCs of some confused targets were visually inspected. However, based on our previous experiences of RSGs LCs (e.g., Kiss et al. 2006; Yang & Jiang 2011, 2012; Soraisam et al. 2018; Ren et al. 2019), it is hard to say whether these targets are truly RSGs or not. More interestingly, two O-Miras at the upper right of the zoomed-out region are classified as both optical and MIR spectroscopic RSGs.

In brief, there is a blurred boundary between AGBs and RSGs, and no efficient way to distinguish between them by

using current data. More data (e.g., spectra with higher resolution and larger wavelength coverage, narrow-filter photometries, multiwavelength time series observations, submillimeter data) are strongly needed to further distinguish between AGBs and RSGs.

Meanwhile, based on the fact that obscured objects would be brighter and redder at the longer wavelengths compared to the shorter wavelengths, we identified one heavily obscured target (big cross) in the entire RSG sample (from Rank -1 to 5) by adopting $K_S > 12.7$ mag or IRAC1 > 12.6 mag (targets were fainter either than the K_S -TRGB or IRAC1-TRGB), $J - \text{IRAC1} \geq 3.0$ mag, and IRAC1 < 10.0 mag (see also next subsection). The obscured target shows high luminosities at the longer wavelengths dominated by the dust emission but dimming at the shorter wavelengths, in particular it is located below the K_S -TRGB. Although it lies in the x-AGBs region at the longer wavelengths, the obscured target is found very close to the RSGs region in the 2MASS CMD and inside the RSGs regions in other CMDs (e.g., *Gaia*, SkyMapper, NSC, which are not shown here), for which it will move along the opposite direction of the reddening vector without the extinction (to be brighter and bluer). Other RSG candidates located in the AGBs regions at the longer wavelengths are similar to the obscured target, that they will be located in the RSG region without the extinction.

3.2. Mid-infrared color-magnitude diagrams

Figure 5 shows four CMDs, with various combinations of MIR and NIR filters. For the IRAC1 versus IRAC1-IRAC2 diagram, the RSG sample mainly shows the negative color index of IRAC1-IRAC2 with a median value of -0.076 , due

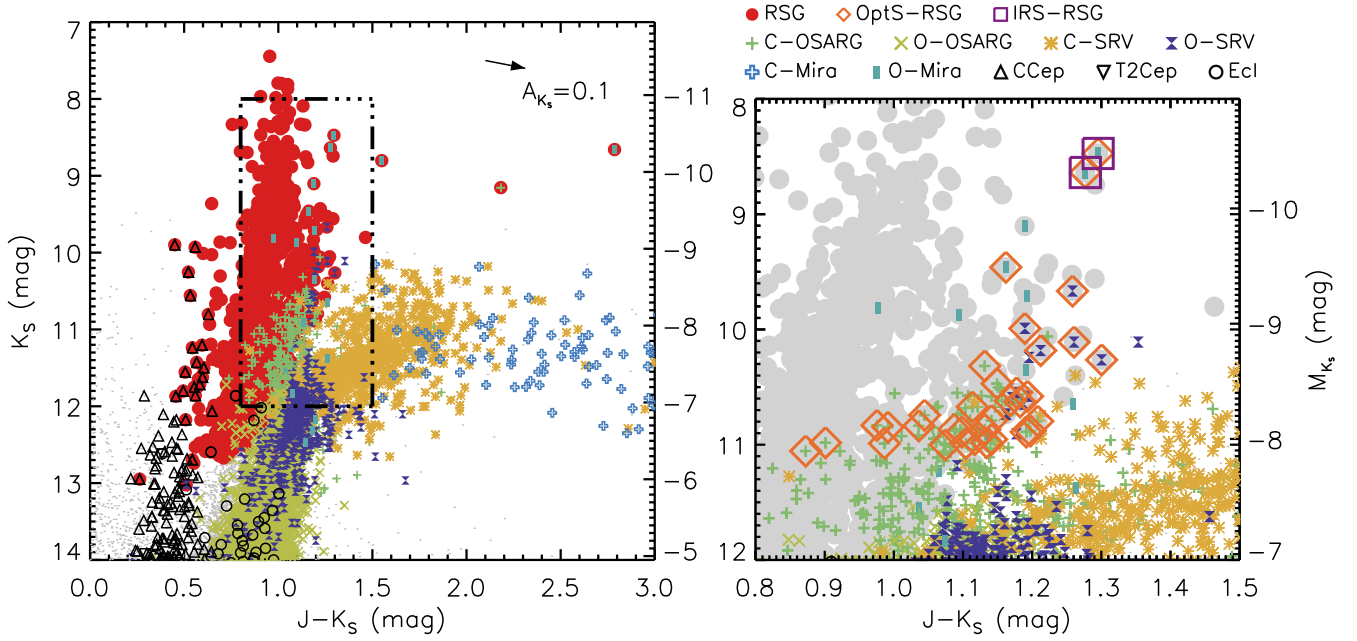


Fig. 4. *Right panel:* same diagram as Fig. 3, but with variable classifications from OGLE. Different types of variables are shown as different symbols. An overlapping of OSARGs, SRVs, and Miras can be seen in the lower half of the zoomed-out region. *Left panel:* same zoomed-out region as Fig. 3, where 24 C-OSARGs, 7 O-SRVs, and 3 O-Miras are optical spectroscopic RSGs (open diamonds). More interestingly, two O-Miras at the upper right are classified as both optical and MIR spectroscopic RSGs (open squares).

Table 1. Numbers of classified variable stars from OGLE.

Class	Subclass	Number	Source
Long Period Variables (LPVs)		8982	O ³ CVS ^(a)
	Carbon-rich OGLE Small Amplitude Red Giants (C-OSARGs)	439	
	Oxygen-rich OSARGs (O-OSARGs)	7417	
	Carbon-rich Semi-Regular Variables (C-SRVs)	644	
	Oxygen-rich SRVs (O-SRVs)	371	
	Carbon-rich Miras (C-Miras)	92	
	Oxygen-rich Miras (O-Miras)	19	
Classical Cepheids (CCeps)		482	O ⁴ CVS ^(b)
Type II Cepheids (T2Ceps)		11	O ⁴ CVS
Eclipsing Binaries (Ecls)		87	O ⁴ CVS

Notes. ^(a)OGLE-III Catalog of Variable Stars. ^(b)OGLE-IV Catalog of Variable Stars.

to the CO absorption around $4.6\mu\text{m}$ (Verhoelst et al. 2009; Britavskiy et al. 2015; Reiter et al. 2015). In particular, the main population of the RSG sample ($\text{IRAC1} \gtrsim 9.5$ mag and $\text{IRAC1} - \text{IRAC2} \lesssim 0$ mag; $\sim 80\%$) shifts slightly bluewards as the luminosity increases, indicating possibly the strengthening of CO absorption. However, this trend turns redwards when targets brighter than $\text{IRAC1} \approx 9.5$ mag (dashed line), which may be due to the enhanced mass loss caused by both luminosity and variability (Yang et al. 2018). At the bright end ($\text{IRAC1} \lesssim 8.5$ mag; dashed line), the trend again turns bluewards, which may be explained by the polycyclic aromatic hydrocarbon (PAH) emission in $3.3\mu\text{m}$ captured by the IRAC1 filter (Buchanan et al. 2006; Verhoelst et al. 2009). More importantly, it seems that only the very bright RSGs will produce PAHs, although this may need further confirmation from the MIR spectroscopy. Notably, there is another branch of targets (also containing many spectroscopic RSGs) at fainter magnitude ($9.3 \lesssim \text{IRAC1} \lesssim 10.0$ mag and $0 \lesssim \text{IRAC1} - \text{IRAC2} \lesssim 0.35$ mag) extended to the x-AGBs region. This branch may be due to the complicated interaction

between PAH, CO, dust, and/or of unknown chemical composition, or, as discussed in previous section, due to the misclassification of AGBs.

In the IRAC4 versus $J - \text{IRAC4}$ diagram, the $J - \text{IRAC4}$ color index is mainly affected by the infrared excess related to the broad $9.7\mu\text{m}$ silicate emission feature, which is attributed to the Si-O stretch resonance and/or the relatively weak $7.6\mu\text{m}$ PAH emission feature captured by the IRAC4 band (Sloan et al. 2008; Bonanos et al. 2009; Boyer et al. 2011). Meanwhile, for the WISE3 versus $K_S - \text{WISE3}$ diagram (for clarity, RSG candidates with WISE3-band signal-to-noise ratio (S/N) less than 10 are shown as red open circles, while background targets from the SMC source catalog with $S/N_{\text{WISE3}} < 10$ are not shown in the diagram), the $K_S - \text{WISE3}$ color index is also affected by the $9.7\mu\text{m}$ feature and/or $18\mu\text{m}$ silicate emission from Si-O-Si bending mode in the SiO_4 tetrahedron (Josselin et al. 2000; Verhoelst et al. 2009; Chen et al. 2016). Both of them can be considered proxies for the MLR. Since oxygen-rich dust shows silicate features at 9.7 and $18\mu\text{m}$ that appear in emission at low

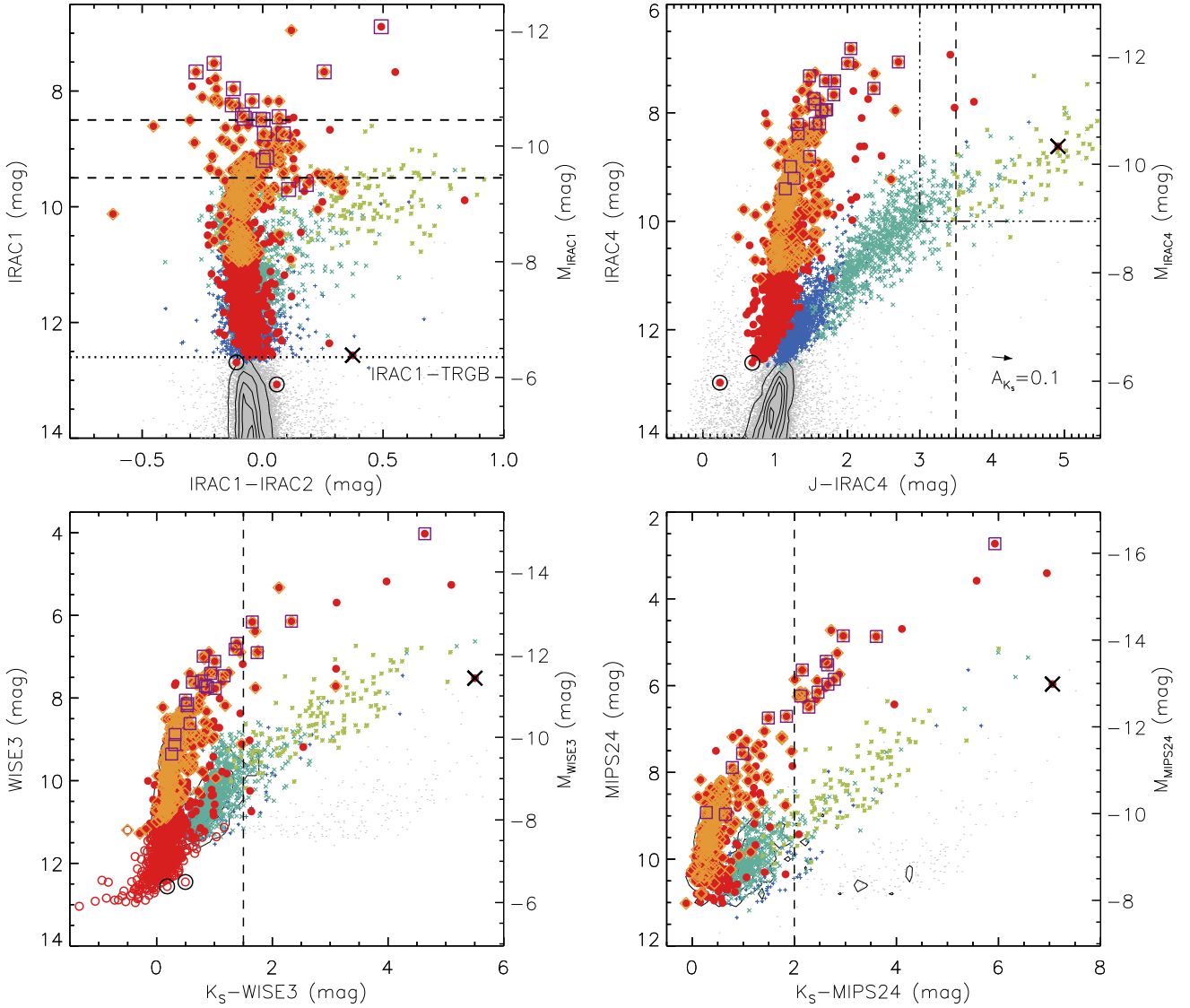


Fig. 5. *Upper left:* IRAC1 vs. IRAC1–IRAC2 diagram. The RSG sample mainly shows negative value of IRAC1–IRAC2 due to the CO absorption around $4.6\ \mu\text{m}$. In particular, it turns bluewards (IRAC1 ≥ 9.5 mag) with CO absorption, redwards ($8.5 \leq \text{IRAC1} \leq 9.5$) with enhanced mass loss due to both luminosity and variability, and again bluewards (IRAC1 ≤ 8.5) with PAH emission, along with the increasing of luminosity. There is another fainter branch ($9.3 \leq \text{IRAC1} \leq 10.0$ mag and $0 \leq \text{IRAC1} - \text{IRAC2} \leq 0.35$ mag) extended to the x-AGBs region with unknown origin. *Upper right:* IRAC4 vs. $J - \text{IRAC4}$ diagram. The dash-dotted lines region indicates the selection criteria for the obscured target. *Bottom left:* WISE3 vs. $K_S - \text{WISE3}$ diagram. For clarity, RSG candidates with $S/N_{\text{WISE3}} < 10$ are shown as red open circles, while background targets from SMC source catalog with $S/N_{\text{WISE3}} < 10$ are not shown in the diagram. The RSGs population shows redder color of $J - \text{IRAC4}$ and $K_S - \text{WISE3}$ along with the increasing of IRAC4/WISE3 luminosity. *Bottom right:* MIPS24 vs. $K_S - \text{MIPS24}$ diagram. The majority of the MIPS24 detected targets are also spectroscopic RSGs. The brightest RSGs candidates form a parallel sequence with respect to the x-AGBs population. The vertical dashed lines indicate the approximate blue boundaries of x-AGBs. See text for details.

optical depths and absorption at high optical depths (i.e., with high MLR; Sylvester et al. 1999; Kemper et al. 2000), it also explains why the obscured and some other RSG candidates are located in the AGBs region at the longer wavelengths (targets with high MLR will become red and faint). In any case, the RSG population shows redder colors of $J - \text{IRAC4}$ and $K_S - \text{WISE3}$ along with the increasing of IRAC4 and WISE3 luminosities, indicating the growth of MLR and circumstellar envelope.

In the MIPS24 versus $K_S - \text{MIPS24}$ diagrams, since the MIPS24 band traces the relatively cold dust continuum with very little contribution from the stellar photosphere, the $K_S - \text{MIPS24}$ color is also a good indicator of MLR. Due to the greater distance compared to the LMC and lower sensitivity at the longer wavelength, the majority of the RSGs candidates remain undetected

in MIPS24 band ($\sim 67\%$) or are only detected with an upper limit in WISE4 band ($\sim 76\%$), while most of the detected targets are also spectroscopic and/or bright RSGs. From the diagram, it can be seen that there are two parallel sequences showing ascending trends in both MIPS24 luminosity and $K_S - \text{MIPS24}$ color, formed by the brightest RSG candidates and x-AGBs, respectively. This likely indicates a similarly high MLR in these stars.

Furthermore, by simultaneously inspecting the last three diagrams, it occurs to us that the brightest RSG candidates are likely having high MLR comparable to the x-AGBs, as x-AGB stars may be experiencing a “superwind” with extreme MLR and a thick dust envelope (van Loon et al. 2006; Boyer et al. 2011; Höfner & Olofsson 2018). This can be seen by comparing the colors (infrared excesses) of the brightest RSG candidates and

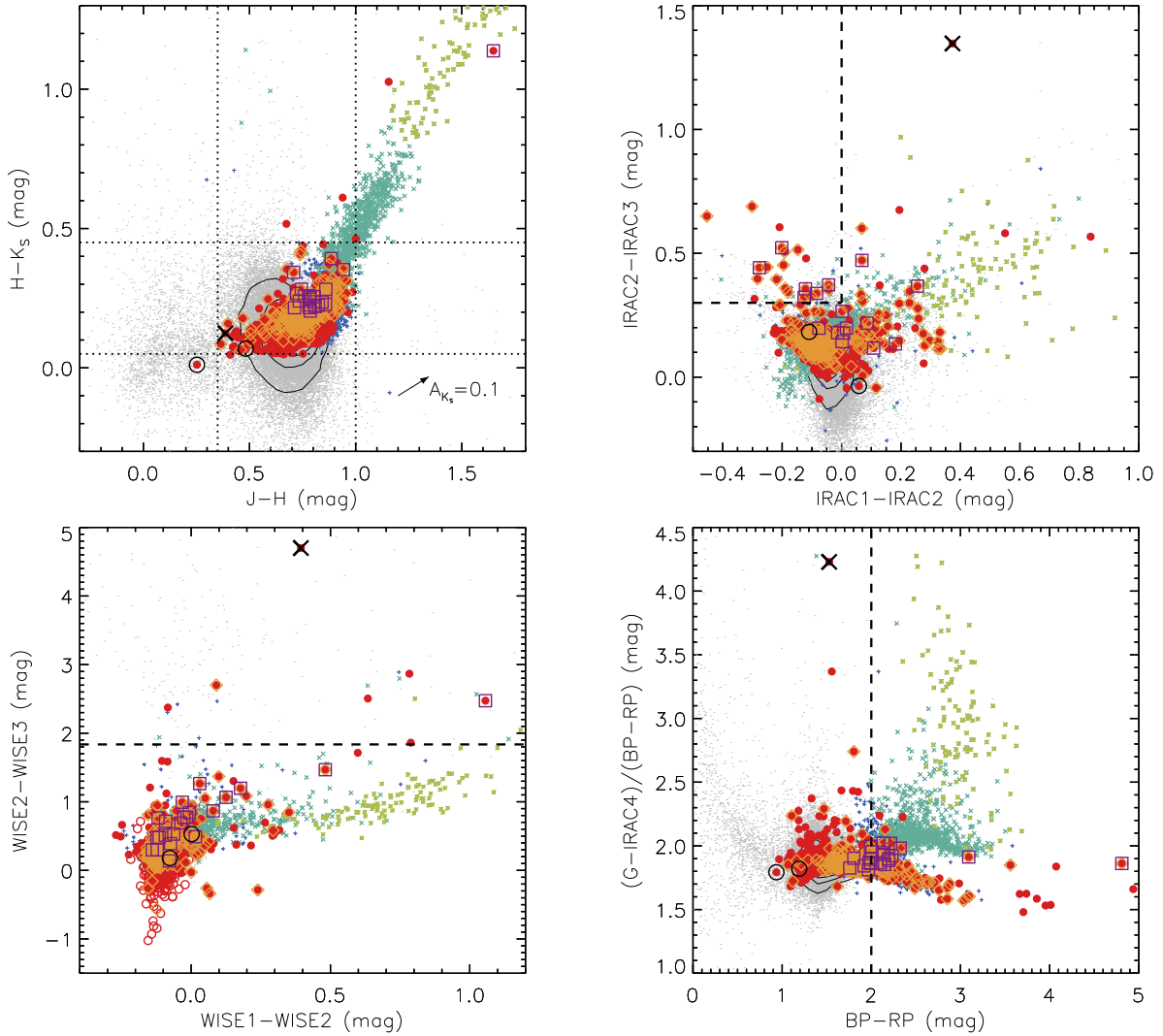


Fig. 6. *Upper left:* 2MASS CCD of $J - H$ vs. $H - K_S$. The RSGs population is clumping within the range of $0.35 \leq J - H \leq 1.0$ and $0.05 \leq H - K_S \leq 0.45$ (dotted lines), and is indistinguishable from the O-AGBs. *Upper right:* IRAC CCD of $IRAC1 - IRAC2$ vs. $IRAC2 - IRAC3$. The previously defined PAH emission region of $IRAC1 - IRAC2 \leq 0$ and $IRAC2 - IRAC3 \geq 0.3$ is shown as dashed lines (Yang et al. 2018). There are only about 4% (after correcting for the completeness) of RSG candidates that show PAH emission features. *Bottom left:* WISE CCD of $WISE1 - WISE2$ vs. $WISE2 - WISE3$. The horizontal dashed line indicates $F_{\nu, WISE2} = F_{\nu, WISE3}$ ($WISE2 - WISE3 = 1.84$), for which there are only seven targets above it. *Bottom right:* optical-MIR color excesses of $BP - RP$ vs. $(G - IRAC4)/(BP - RP)$. RSG candidates (and O-AGBs), C-AGBs, and x-AGBs having lowest, moderate, and highest ratio of $(G - IRAC4)/(BP - RP)$ at $BP - RP \geq 2.0$ (vertical dashed line), respectively.

x-AGB population. For example, in the $IRAC4$ versus $J - IRAC4$ diagram, the x-AGBs are redder than $J - IRAC4 \approx 3.5$ mag, where only two targets from our sample have the similar colors. Proceeding to longer wavelengths, the number of brightest RSG candidates similar to x-AGB color increases to 18 ($K_S - WISE3 \gtrsim 1.5$ mag) and 30 ($K_S - MIPS24 \gtrsim 2.0$ mag), respectively. The inconsistency between infrared excesses of the shorter ($8 \mu\text{m}$) and longer (12 and $22 \mu\text{m}$) wavelengths suggests that it may not be enough to characterize the MLR of brightest RSGs even with the wavelength as long as $8 \mu\text{m}$.

In total, there were 1240 targets remaining in our RSG sample. No further constraints were made on the CMDs as we did in Yang et al. (2018). This is due to three factors. First, all the RSG candidates have already been constrained either by the astrometric parameters and the evolutionary models, or the radial velocities and spectral/luminosity types, which indicates that their luminosities and colors are well determined and there is almost no foreground contamination. Second, there are too many

combinations of filters (50 optical and infrared filters) and not all the combinations are efficient, as the completeness and sky coverage are different for different datasets. Third, the optical filters suffer more from extinction and reddening than the infrared filters, which is even worse for the targets with higher MLR.

3.3. Color-color diagrams

We also investigated the distribution of RSGs population on the color-color diagrams (CCDs). Generally speaking, stars will move along the direction of reddening vector due to the interstellar reddening but deviate from it due to the circumstellar reddening (Bonanos et al. 2010; Wachter et al. 2010; Messineo et al. 2012).

The upper left panel of Fig. 6 shows the 2MASS CCD of $J - H$ versus $H - K_S$. Even with our extended sample size, it is still the same as in Yang et al. (2018) and previous studies. The RSGs population clumps within the range of $0.35 \leq J - H \leq 1.0$

and $0.05 \lesssim H - K_S \lesssim 0.45$ (dotted lines), which is in agreement with Rayner et al. (2009). Moreover, it is indistinguishable from the O-AGBs due to the similar intrinsic temperatures and chemical compositions as well as the low-luminosity RGBs, while C-AGBs and x-AGBs are distinguishable and show different tendencies due to different chemical composition and/or MLRs.

The upper right and bottom left panels of Fig. 6 show IRAC (IRAC1–IRAC2 versus IRAC2–IRAC3) and WISE (WISE1–WISE2 versus WISE2–WISE3) CCDs, respectively. For both IRAC and WISE CCDs, as expected, the majority of RSG candidates show blue color (<0) in IRAC1–IRAC2 and WISE1–WISE2 due to CO absorption as mentioned before. In IRAC1–IRAC2 versus IRAC2–IRAC3 diagram, we indicated previously defined PAH emission region of IRAC1–IRAC2 ≤ 0 and IRAC2–IRAC3 ≥ 0.3 shown as dashed lines (Yang et al. 2018). However, for the SMC, only about 4% (after correcting for the completeness, which is based on the estimation from the results of Yang et al. 2018 and our source catalog of the LMC; Yang 2019) of RSG candidates show PAH emission features, which is much lower than the Milky Way and LMC ($\sim 15\%$; Verhoelst et al. 2009; Yang et al. 2018). This is likely consistent with the strong metallicity dependence of PAH abundance due to the shattering of carbonaceous grains being the source of PAHs, which may be caused by the harder and more intense radiation fields in low-metallicity environments and/or the enhanced SN activity (Engelbracht et al. 2005; O’Halloran et al. 2006; Draine et al. 2007; Seok et al. 2014; Shivaeei et al. 2017). Even so, most of the scenarios are presumably applied on a much larger scale dominated by the interstellar medium (ISM), according to the observation of nearby and high-redshift galaxies. Meanwhile, the mechanism for individual stars, especially for PAHs in O-rich RSGs, is still unclear. Moreover, since the presence of PAHs in the ISM could not be explained entirely by the C-AGBs (Matsuura et al. 2013), the contribution of RSGs might be considered, and further MIR spectroscopy is needed to understand the scenario. For the WISE1–WISE2 versus WISE2–WISE3 diagram, compared to the LMC, there are only seven targets showing extreme MIR excess in terms of WISE2–WISE3 ≥ 1.84 ($F_{\nu, \text{WISE2}} = F_{\nu, \text{WISE3}}$; dashed line). It is likely due to the metallicity dependence of dust-driven outflows, as a lower metallicity may result in a lower mass of dust grains, and consequently, a smaller integrated cross section for radiation pressure on dust grains and a lower MLR (Justtanont & Tielens 1992; Marshall et al. 2004; Maun & Josselin 2011).

Finally, the bottom right panel of Fig. 6 shows optical-MIR color excesses of $BP - RP$ versus $(G - \text{IRAC4}) / (BP - RP)$, which simply reflects the relation between the photosphere or spectral type ($BP - RP$) and the reddening or dust excess ($G - \text{IRAC4}$). It can be seen from the diagram that targets with $BP - RP \geq 2.0$ are split into three groups, where RSG candidates (and O-AGBs), C-AGBs, and x-AGBs have lowest, moderate, and highest ratio of $(G - \text{IRAC4}) / (BP - RP)$, respectively, which may be caused by the different chemical composition and/or high MLR.

3.4. Mid-infrared variability

As stated in Yang et al. (2018) and other studies (Wood et al. 1983; Kiss et al. 2006; Groenewegen et al. 2009; Yang & Jiang 2011, 2012), RSGs typically have lower variability in the same magnitude range compared to AGBs, which can be used as an indicator to separate them. We analyzed the long-term epoch-binned MIR time series data from WISE for our RSG sample with 1240 targets. For each target, the median value of single-epoch MADs (approximately five to ten days for each epoch)

was also calculated as an estimation of short-term variability. Among them, 48 targets ($\sim 4\%$) do not have MIR variability statistics, which is likely due to the quality cuts applied when retrieving the time series data (see more details about the binning method and WISE photometric quality cuts in Sect. 3 of Yang et al. 2018). Even though our SMC source catalog included other variability statistics, they were neither relatively complete in the spatial or magnitude range, nor homogeneous in the sampling, which left the WISE data as the only choice we had. The saturation problem for WISE data was discussed in the Sect. 4.4 of Yang et al. (2018), which was more mitigated in the SMC due to the greater distance compared to the LMC.

Figure 7 shows the median absolute deviation (MAD), which is a robust measurement of variability against outliers (Rousseeuw & Croux 1993), versus median magnitude in WISE1 band (left) and the 2MASS CMD (right). From the left panel it can be seen that the MIR variability of the RSG sample increases with luminosity. In total, $\sim 21\%$ of targets have $\text{MAD}_{\text{WISE1}} > 0.01$ mag (dotted line), which is at least three times higher than the robust sigma of photometric error (~ 0.003 mag in WISE1 band) and most likely indicates real variability considering the binned data we use (see also the inset, which shows only the RSG sample with the limit of $\text{MAD}_{\text{WISE1}} = 0.01$ mag in the range of $13.0 < \text{Median}_{\text{WISE1}} < 7.0$ mag and $0 < \text{MAD}_{\text{WISE1}} < 0.025$ mag). The rest of the targets are considered variability undetected or unreliable. Meanwhile, only a few targets ($\sim 2\%$) show a large variation (e.g., $\text{MAD} > 0.1$ mag; dashed line) with $\text{Median}_{\text{MAD}} \approx 0.2$ mag. For the brighter targets (e.g., $\text{Median}_{\text{WISE1}} < 9.0$ mag) the median MAD is about 0.03 mag, while the fainter targets (e.g., $\text{Median}_{\text{WISE1}} \geq 9.0$ mag) show much less variation ($\text{Median}_{\text{MAD}} \approx 0.005$ mag). The normalized histogram (NC) indicates the range of $0 < \text{MAD}_{\text{WISE1}} < 0.05$ mag, where the median values and histograms of all (gray), brighter (red), and fainter targets (purple) are shown.

Even through RSGs typically have semi-regular variabilities and moderate amplitudes, there are still some exceptions showing significant variabilities in different magnitude ranges (Kiss et al. 2006; Yang & Jiang 2012; Soraisam et al. 2018; Ren et al. 2019). Thus, we were only able to identify some extreme outliers based on the variabilities, luminosities, and colors at the same time. We separated the RSG sample into two subsamples. The “risky” subsample represented high-variability and red targets with $\text{MAD} > 0.1$ mag and $J - K_S$ color redder than the median value of the RSG sample ($J - K_S = 0.89$ mag). It was considered more risky to be contaminated by the AGBs since compared to the RSGs, AGBs would have redder color and higher variability. The “safe” subsample represented low variability ($\text{MAD} \leq 0.1$ mag) or blue targets ($\text{MAD} > 0.1$ mag and $J - K_S \leq 0.89$ mag). For the safe subsample, in the fainter magnitude range (e.g., $\text{WISE1} \gtrsim 11.0$ or $K_S \gtrsim 11.0$ mag), simultaneous inspection of both panels of Fig. 7 indicates that the majority of targets with relatively higher variabilities are located in the blue end of the RSG sample, which is reasonable since they are likely to be the progenitors or descendants of RSGs crossing the instability strip, and may be classified as CCeps as shown in the left panel of Fig. 4. Meanwhile, in the brighter magnitude range (e.g., $\text{WISE1} < 11.0$ or $K_S < 11.0$ mag), a few spectroscopic RSGs also present excessive variabilities compared to the main sample of RSGs (as discussed before, the true nature of some spectroscopic RSGs is still in debate), for which other studies also indicate that the peak-to-peak amplitudes of some RSGs may reach up to four magnitudes in the optical (Kiss et al. 2006; Yang & Jiang 2011, 2012; Chatys et al. 2019; Ren et al. 2019) and prevent us from constraining the

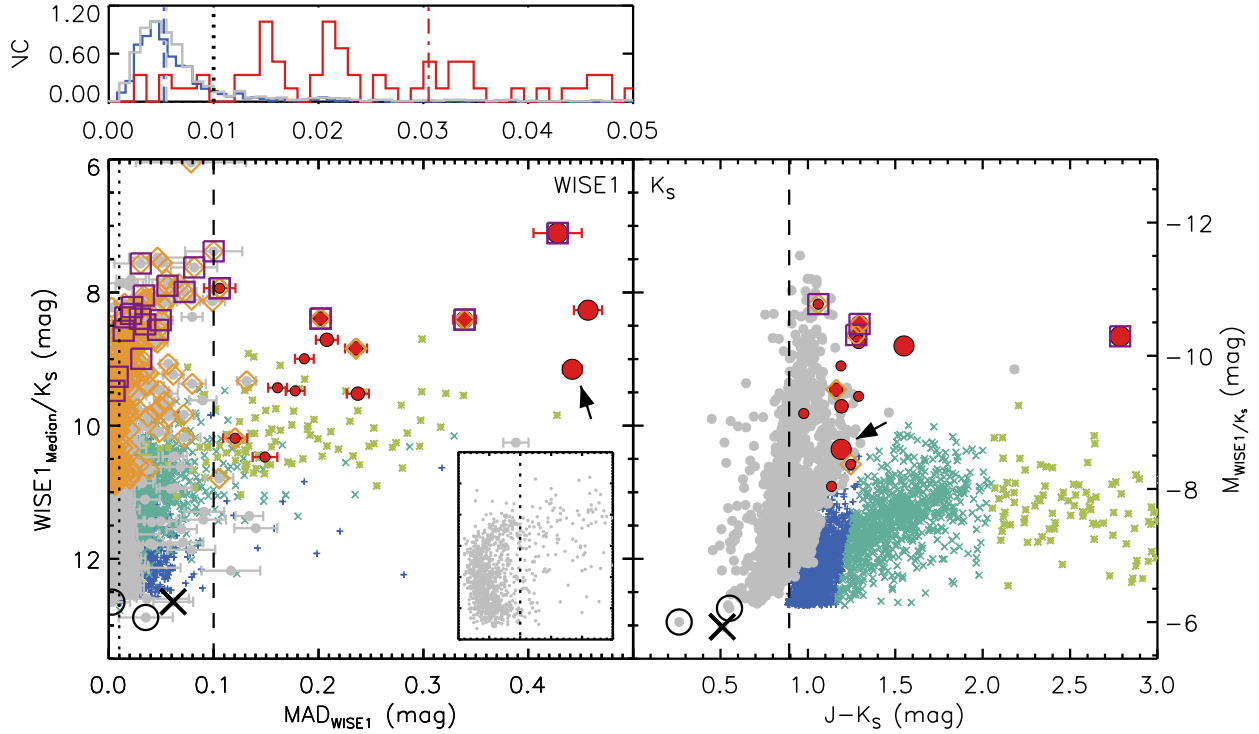


Fig. 7. *Left:* MAD vs. median magnitude in WISE1 bands. For convenience, the diagram only shows the RSG sample and AGB populations. The median value of single-epoch MADs (each epoch is approximately five to ten days) of each target is shown as the error. The optical and MIR spectroscopic RSGs are shown as open diamonds and open squares, respectively. The MIR variability of RSG sample increases along with luminosity. In total, $\sim 21\%$ of targets have $MAD_{WISE1} > 0.01$ mag (dotted line) and $\sim 2\%$ have $MAD > 0.1$ mag (dashed line). The inset shows only the RSG sample with the limit of $MAD_{WISE1} = 0.01$ mag in the range of $13.0 < Median_{WISE1} < 7.0$ mag and $0 < MAD_{WISE1} < 0.025$ mag. The RSG sample is separated into two subsamples. One subsample represents high-variability and red targets with $Median_{MAD} > 0.1$ mag and $J - K_S > 0.89$ mag, which may be more at risk of being contaminated by AGBs (the increasing symbol sizes indicating the increasing variabilities). The other subsample (gray) represents low variability ($MAD \leq 0.1$ mag) or blue ($MAD > 0.1$ mag and $J - K_S \leq 0.89$ mag) targets. One M5e AGBs is identified (arrows) and excluded from our RSG sample, based on its significant variability with moderate magnitude. The normalized histogram (NC; upper left) indicates the range of $0 < MAD_{WISE1} < 0.05$ mag, where the distributions of all (gray), brighter ($Median_{WISE1} < 9.0$ mag; red), and fainter targets ($Median_{WISE1} \geq 9.0$ mag; blue) are shown (for clarity, slightly different bin sizes are used for different groups). The dash-dotted lines indicate the median values of corresponding groups. See text for details.

Table 2. Final sample of 1239 red supergiant star candidates in the SMC.

ID	RA (J2000) (deg)	Dec (J2000) (deg)	2MASS_J (mag)	e_{2MASS_J} (mag)	...	OGLE_Ecl_DS (mag)	Rank
124	4.368634	-73.428555	12.497	0.022	...		2
236	4.921237	-73.353052	11.675	0.022	...		4
240	4.952093	-73.588549	12.672	0.024	...		2
635	5.800023	-72.390737	12.920	0.029	...		3
747	5.977038	-73.639891	12.253	0.023	...		2
...

Notes. This table is available in its entirety at CDS. A portion is shown here for guidance regarding its form and content.

sample further. However, the contamination of AGBs should be small compared to the fainter magnitudes, while as the luminosity increases the contamination will be rapidly decreased. For the risky subsample (14 targets in total, 6 of which are spectroscopic RSGs), targets are shown in both panels of Fig. 7 with increasing symbol sizes indicating the increasing variabilities. The majority of the targets show increasing variabilities along with the increasing luminosities, except one (indicated by the arrows in the panels) that shows significant variability with moderate magnitude. Further investigation indicated that it was a M5e AGB star (Whitelock et al. 1989). We excluded this target from our

RSG sample. Consequently, there are 1239 RSG candidates in the final sample as listed in the Table 2 (see Table 3 of Yang et al. 2019 regarding the form and content of the table).

We note that there may still be a small contamination in our RSG sample from the AGBs and/or RGBs, especially at the faint and/or red end, which is inevitable and may not be disentangled solely based on the photometric data. Moreover, as mentioned before, until the next generation of large-scale spectroscopic data becomes available, there is no absolutely way to separate AGBs from RSGs. However, since it is constrained by several factors (e.g., astrometry, evolutionary model, luminosity, color,

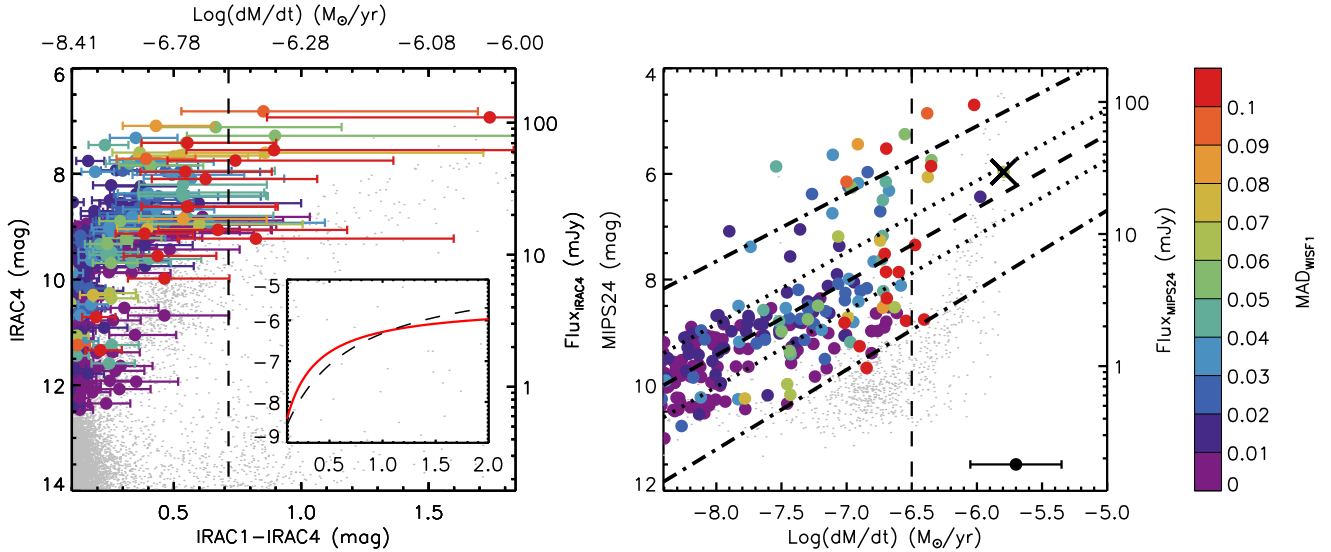


Fig. 8. IRAC4 vs. IRAC1–IRAC4 (*left*) and MIPS24 vs. MLR (*right*) diagrams color-coded with WISE1-band variability (same below). The IRAC1–IRAC4 color is converted to the MLR by using a modified algorithm from [Groenewegen & Sloan \(2018\)](#), where the inset shows the comparison between the new (red solid line) and old (black dashed line) algorithms (*x*-axis is the IRAC1–IRAC4 color and *y*-axis is the MLR). The error bars show typical error of 0.35 dex. Most of the targets appear to have MLR below $\sim 10^{-6.5} M_{\odot} \text{ yr}^{-1}$ (vertical dashed line; for convenience, two targets showing substantial MLR, e.g., $> 10^{-6.0} M_{\odot} \text{ yr}^{-1}$, are not shown in the IRAC4 vs. IRAC1–IRAC4 diagram). There is a linear relation (dashed line) between MIPS24 magnitude and MLR, while the dotted lines and dash-dotted lines indicate the 1σ and 3σ uncertainties, respectively. Moreover, some targets lying above the upper limit of 3σ may be related to episodic mass loss events during the RSGs phase.

variability), we are confident that, statistically, our sample is sufficient to represent the entire RSGs population in the SMC up to now.

4. Discussion

4.1. Mass loss rate, luminosity, and variability of RSGs in the SMC

Following [Yang et al. \(2018\)](#), we analyzed the relation between MLR, luminosity, and variability of the final sample of RSGs in the SMC. Figure 8 shows the regimes dominated by the relatively long wavelengths, the IRAC4 versus IRAC1–IRAC4 (left) and MIPS24 versus MLR (right) diagrams color-coded with WISE1-band variability. The IRAC4 ($8.0 \mu\text{m}$) and MIPS24 ($24 \mu\text{m}$) bands represent the relatively hot and cold dust components, respectively. The IRAC1–IRAC4 color was converted to the MLR by using an algorithm for O-rich supergiant stars as

$$\text{Log } \dot{M} = -5.598 - \frac{0.817}{(\text{IRAC1} - \text{IRAC4}) + 0.191}, \quad (1)$$

derived by [Groenewegen & Sloan \(2018\)](#), based on a large sample of evolved stars in several Local Group galaxies with a variety of metallicities and star-formation histories. The typical uncertainty of $\text{Log } \dot{M}$ is about 0.35 dex with color constraint (the algorithm may not be available for targets with $\text{IRAC1} - \text{IRAC4} < 0.1$ mag due to the quick drop of MLR in the bluest color). We note that this algorithm only considers O-rich RSGs and different from the original one used in the paper. This is mostly because the original algorithm treats AGBs and RSGs together as M-type stars, for which there is an apparent split in the MLR for AGBs and RSGs, with the RSGs usually showing higher MLRs. Moreover, when considering only RSGs, the error is also smaller (~ 0.35 dex versus originally ~ 0.49 dex; [Martin Groenewegen](#), private communication). The inset in Fig. 8 shows the comparison between the new and old algorithms.

From the two diagrams, most of the targets appear to have MLR below $\sim 10^{-6.5} M_{\odot} \text{ yr}^{-1}$ (vertical dashed lines), while targets with higher MLR are also the ones with higher variability and higher luminosity, which may be due to the contribution from both variability and luminosity ([Josselin & Plez 2007](#); [van Loon et al. 2008](#); [Yoon & Cantiello 2010](#); [Yang et al. 2018](#)). Only two targets in the diagrams show substantial MLR ($> 10^{-6.0} M_{\odot} \text{ yr}^{-1}$). For the IRAC4 versus IRAC1–IRAC4 diagram, there are 382 valid targets ($\sim 32\%$) redder than $\text{IRAC1} - \text{IRAC4} = 0.1$ mag. Fifty-five of them ($\sim 14\%$) are brighter than $\text{IRAC4} = 8.5$ mag ($\text{Flux}_{\text{IRAC4}} \gtrsim 25.84$ mJy). For the MIPS24 versus MLR diagram, there are 231 valid targets redder than $\text{IRAC1} - \text{IRAC4} = 0.1$ mag. Forty-one targets ($\sim 18\%$) are brighter than $\text{MIPS24} = 8.0$ mag ($\text{Flux}_{\text{MIPS24}} \gtrsim 4.52$ mJy).

As can be seen in the MIPS24 versus MLR diagram, there is a linear relation (dashed line) between MIPS24 magnitude and MLR if we adopt the targets with $\text{IRAC1} - \text{IRAC4} \geq 0.1$ mag as

$$\text{MIPS24} = (-1.37 \pm 0.04) \times \text{Log } \dot{M} + (-1.52 \pm 0.29), \quad (2)$$

while the dotted lines and dash-dotted lines indicate the 1σ and 3σ uncertainties (the observational error of MIPS24 band and a constant error of ~ 0.35 dex in the MLR are both taken into account), respectively. This linear relation can be understood as the result of the degeneracy of the variability and luminosity in relation to boosting the MLR, as mentioned before, since the linear relation here corresponds to an exponential relation in the flux domain. In other words, the MIPS24 ($24 \mu\text{m}$) flux grows exponentially along with the increase in the brightness and variability of the star. Moreover, we also note that there are some targets lying above the upper limit of 3σ , which may be related to episodic mass loss events during the RSGs phase ([Smith et al. 2009](#); [Smith 2014](#)) despite their moderate errors.

Based on the derived MLR, we are able to roughly estimate the gas and dust budget produced by the RSG population in the

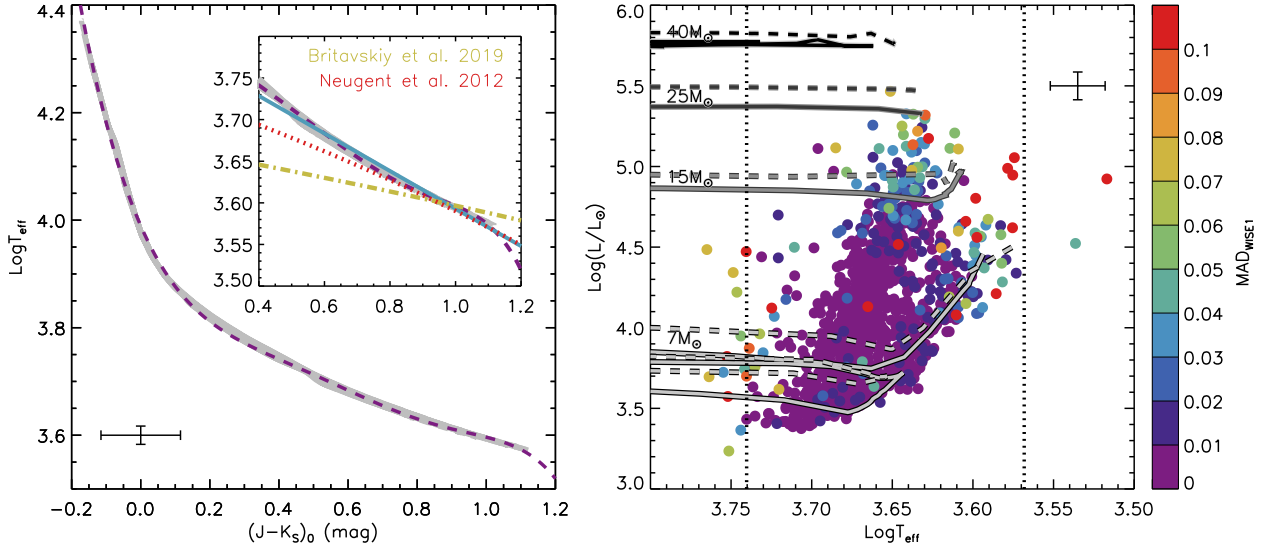


Fig. 9. *Left:* T_{eff} vs. reddening-free $J - K_S$ color ($(J - K_S)_0$) over the range of $3.57 \leq \text{Log } T_{\text{eff}} \leq 4.35$ and $-0.16 \leq (J - K_S)_0 \leq 1.13$ derived from the MIST models. A sixth-order polynomial fitting is shown as a dashed line, which works very well, except at the very red end. The inset shows the range of $3.5 \leq \text{Log } T_{\text{eff}} \leq 3.8$ and $0.4 \leq (J - K_S)_0 \leq 1.2$, where a linear fitting is adopted shown as solid line instead of the polynomial fitting. Results from Britavskiy et al. (2019) (dash-dotted line) and Neugent et al. (2012) (dotted line) are also shown in the diagram. Our result is almost identical to that of Neugent et al. (2012) in the range of $0.8 \leq (J - K_S)_0 \leq 1.2$. *Right:* RSG sample (color-coded with WISE1-band variability) overlapped with color-coded non-rotation (solid lines) and rotation ($V/V_C = 0.40$; dashed lines) Geneva evolutionary tracks of 7 to $40 M_{\odot}$ at $Z = 0.002$. Vertical dotted lines indicate the T_{eff} range of 3700–5700 K for the RSG sample. The vast majority of targets selected by MIST model are following the Geneva tracks, and a few outliers can be explained by the combination of variability and reddening. Error bars show the typical errors of ~ 0.017 dex in $\text{Log } T_{\text{eff}}$ and ~ 0.086 dex in $\text{Log}(L/L_{\odot})$.

SMC. For our sample, a total of about $\sim 2.2^{+2.7}_{-1.2} \times 10^{-5} M_{\odot} \text{ yr}^{-1}$ is counted for 382 targets with $\text{IRAC1} - \text{IRAC4} \geq 0.1$ (the rest of the 818 targets with $\text{IRAC1} - \text{IRAC4} < 0.1$ will contribute about $\leq 1.0 \times 10^{-7} M_{\odot} \text{ yr}^{-1}$, if we adopt $\sim 1.0 \times 10^{-10} M_{\odot} \text{ yr}^{-1}$ as the average MLR, due to the quick drop in MLR in the bluest color; Groenewegen & Sloan 2018). Among them, about 12% of the MLR ($\sim 2.7^{+3.3}_{-1.5} \times 10^{-6} M_{\odot} \text{ yr}^{-1}$) originates from two extremely dusty RSG candidates with $\text{MLR} > 10^{-6} M_{\odot} \text{ yr}^{-1}$. Moreover, considering the saturation problems in the IRAC4 band (two targets with $J - K_S > 2.0$ are saturated in IRAC4 band) and the incompleteness of our sample, the total MLR of the RSG population could be even higher. Even for the most conservative case where the derived MLR is overestimated by one order of magnitude, and not considering the extreme dusty RSG candidates, the total MLR of the RSG population would still be around $\sim 1.9^{+2.4}_{-1.1} \times 10^{-6} M_{\odot} \text{ yr}^{-1}$. Since the gas-to-dust ratio (GDR) in Groenewegen & Sloan (2018) is taken as a constant value of 200, this MLR can be transfer to a dust-production rate of $\sim 1.0^{+1.2}_{-0.5} \times 10^{-8} M_{\odot} \text{ yr}^{-1}$, which is $\sim 30\%$ of Boyer et al. (2012) and $\sim 20\%$ of Srinivasan et al. (2016). However, considering the large uncertainty on the GDR, the results still can be considered comparable, and the discrepancies could be attributed to differences in sample sizes, adopted optical constants, and details in the radiative transfer modeling (Groenewegen & Sloan 2018; see also their Sect. 6.1). We also note that the sample of Groenewegen & Sloan (2018) used to derive the relation between $\text{IRAC1} - \text{IRAC4}$ color and MLR contains very few RSGs with $\text{IRAC1} - \text{IRAC4} > 1.5$ mag, indicating that the MLR of extreme red objects (e.g., the obscured targets) may be underestimated. Moreover, instead of the overestimation as we presumed in the most conservative case, the $\text{IRAC1} - \text{IRAC4}$ color may underestimate the MLR of the brightest RSGs as mentioned in Sect. 3.2 (the small difference between $J - \text{IRAC4}$ and $\text{IRAC1} - \text{IRAC4}$ colors can be ignored), so that the total MLR would be

even higher. The detailed analysis of MLR of RSGs in the SMC will be presented in a future paper.

4.2. Geneva evolutionary model of RSGs at the SMC metallicity

We also compared our final RSG sample with the Geneva stellar evolutionary tracks at the metallicity of $Z = 0.002$ (Georgy et al. 2013). The first step was to convert the observed parameters into physical quantities, namely from the magnitudes and colors to the luminosity and T_{eff} . We adopted a constant bolometric correction of $\text{BC}_{K_S} = 2.69 \pm 0.06$ (Davies et al. 2013) to convert K_S -band magnitude into luminosity because BC_{K_S} of RSGs is independent of IR color with small uncertainty (about 15–25%; Buchanan et al. 2006; Davies et al. 2013). There may be a concern that this BC_{K_S} is derived from RSGs with $\text{Log}(L/L_{\odot}) \geq 4.6$, and here is extrapolated down by about one order of magnitude. However, as discussed in Davies et al. (2010), throughout the mass range of RSGs the pressure scale height remains largely unchanged. Moreover, we compared it before with another BC derived by Neugent et al. (2012), which gave approximately the same result within the error range down to $\text{Log}(L/L_{\odot}) \approx 4.0$, except at the very faint red end (see also Fig. 19 of Yang et al. 2018). Meanwhile, in our sample, we only selected targets with Ranks of -1 to 3 , excluding most of the ambiguous targets at the faint red end. In that sense, the result can be considered acceptable. The conversion between color and T_{eff} is more difficult, since most established relations are used for higher metallicity environments and also derived based on a relatively small sample size (Levesque et al. 2006; Neugent et al. 2012; Tabernero et al. 2018; Britavskiy et al. 2019). Thus, we derived the relation between color and T_{eff} by taking advantage of the MIST evolutionary tracks and synthetic photometry. The left panel of Fig. 9 shows the T_{eff} versus reddening-free $J - K_S$

color $((J - K_S)_0)$ over the range of $3.57 \leq \text{Log } T_{\text{eff}} \leq 4.35$ and $-0.16 \leq (J - K_S)_0 \leq 1.13$ derived from the MIST model. We fitted a sixth-order polynomial shown as the blue dashed line to the data as

$$\begin{aligned} \text{Log } T_{\text{eff}} = & -0.71(J - K_S)_0^6 + 0.41(J - K_S)_0^5 + 3.30(J - K_S)_0^4 \\ & - 5.85(J - K_S)_0^3 + 3.92(J - K_S)_0^2 - 1.47(J - K_S)_0 \\ & + 3.99, \end{aligned} \quad (3)$$

which worked very well, except at the very red end. The inset shows the range of $3.5 \leq \text{Log } T_{\text{eff}} \leq 3.8$ and $0.4 \leq (J - K_S)_0 \leq 1.2$ where the majority of RSGs are supposed to be located. It can be seen that the relation is almost linear within the range and the polynomial fitting largely underestimate the T_{eff} at the very red end (e.g., $(J - K_S)_0 \approx 1.2$). Alternatively, a linear relation shown as the blue solid line was fitted for this range as

$$\text{Log } T_{\text{eff}} = -0.23(J - K_S)_0 + 3.82, \quad (4)$$

and adopted to convert the observed $J - K_S$ color to T_{eff} with reddening correction. Meanwhile, the results from [Britavskiy et al. \(2019\)](#) and [Neugent et al. \(2012\)](#) are also shown in the diagram. Our result is almost identical to [Neugent et al. \(2012\)](#) in the range of $0.8 \leq (J - K_S)_0 \leq 1.2$, where their sample is located, proving that our fitting is appropriate. The difference between the studies is likely due to different metallicities, sample size, and the treatment of parameters in the models.

The typical uncertainty in $J - K_S$ is ~ 0.033 mag. In combination with uncertainties from the reddening (e.g., 50% uncertainty of $E(J - K_S)$ as ~ 0.11 mag) and variability (assuming that 2MASS bands have a typical variability of ~ 0.01 mag, similar to the WISE1 band), this propagates to an error of ~ 0.017 dex in $\text{Log } T_{\text{eff}}$. For $\text{Log}(L/L_\odot)$, an error of ~ 0.086 dex originates from the uncertainty of ~ 0.06 mag in BC_{K_S} , the typical uncertainty of ~ 0.022 mag in K_S , ~ 0.01 mag of variability, ~ 0.05 mag for 50% uncertainty of extinction, and ~ 0.2 mag for 50% uncertainty of the depth in 3D structure of the SMC. The dominant factors of errors for $\text{Log } T_{\text{eff}}$ and $\text{Log}(L/L_\odot)$ come from the reddening and 3D structure of the SMC, respectively. More accurate correction for each individual target cannot be done without precise measurements of the distance and local extinction or reddening. The corresponding errors are shown in both panels of the Fig. 9.

The right panel of Fig. 9 shows our RSG sample (color-coded with WISE1-band variability) overlapped with color-coded non-rotation (solid lines) and rotation ($V/V_C = 0.40$; dashed lines) Geneva evolutionary tracks of 7 to $40 M_\odot$ at $Z = 0.002$. We adopted a color excess of $E(J - K_S) = 0.212$ ($A_{K_S} = 0.1$ mag, $A_J/A_{K_S} = 3.12$ and $A_{K_S}/A_V \approx 0.1$) for de-reddening ([Wang & Chen 2019](#)). It should be noted that for the reddest RSG candidates, which may be very close to the star formation region or largely self-obscured, the reddening can be much greater. From the diagram, it can be seen that the vast majority of targets selected by MIST model follow the Geneva tracks, proving that our conversion is appropriate. The T_{eff} range of the RSG sample spanning around 3700–5700 K (dotted lines). We note that at the bright end there is only one target above $25 M_\odot$ track. However, this also could be due to the high extinction and/or variability of the obscured RSGs, like the outliers on the upper right region of the diagram. At the faint end, by using BC from [Davies et al. \(2013\)](#) other than the MIST BC table, targets still reach down to the $7 M_\odot$ track within the error range, indicating a lower initial mass limit of $\sim 7 M_\odot$ for the RSG population as found in [Yang et al. \(2019\)](#). Meanwhile, a few outliers that deviate largely from the tracks can be explained by the combination of reddening and variability as mentioned in [Yang et al. \(2018\)](#).

4.3. Comparison of RSGs populations between the SMC and LMC

To better understand the relation between metallicity and other physical properties of RSGs, we compared the RSG sample in the LMC from [Yang et al. \(2018\)](#) and the final RSG sample in the SMC. It is important to note that [Yang et al. \(2018\)](#) was published before *Gaia* DR2 released, for which we were only able to retrieve a small sample of the RSGs in the LMC confirmed either by spectroscopy or photometry from previous studies. After *Gaia* DR2 was released, a quick calculation using the same method as [Yang et al. \(2019\)](#) indicated that the ratio of the RSG sample from [Yang et al. \(2018\)](#) to the entire RSGs population in the LMC was higher than we thought (about 20–25% instead of 10–15%, mainly due to the reduced foreground contamination), but was still not very representative. Thus, the comparison between the SMC and LMC presented here only indicates the general difference between these two galaxies.

Figure 10 shows multiple CMDs from NIR to MIR bands (there is no optical data from [Yang et al. 2018](#)). A distance modulus of 18.493 ± 0.055 for the LMC is adopted ([Pietrzyński et al. 2013](#)). For convenience, there are offsets of -0.5 mag in the upper row and -1.0 mag in the bottom row for the color indexes of the SMC sample, while offsets of $+0.5$ mag and $+1.0$ mag for the LMC sample, respectively (contours are not offset). It can be seen that the LMC sample is not magnitude-completed and lacks a large number of fainter and bluer targets. However, considering the upper parts of both the SMC and the LMC sample with comparable magnitudes, there is still a visible difference. Thus, in order to minimize the influence of incompleteness of the LMC sample and not exaggerate the effect of metallicity, we compared the median values of each color index (vertical dashed lines; blue for the SMC and yellow for the LMC) with the same limiting magnitude in both the SMC and the LMC (horizontal dashed lines) as listed in Table 3. For the M_{K_S} versus $J - K_S$ diagram where the stellar photospheric emission remains dominant, the SMC sample shows bluer color than the LMC sample due to the shifting of average spectral type of RSGs towards earlier types at lower metallicities ([Elias & Frogel 1985](#); [Massey & Olsen 2003](#); [Levesque et al. 2006](#); [Levesque & Massey 2012](#); [Dorda et al. 2016](#)). For $M_{\text{IRAC}2}$ versus $\text{IRAC}1\text{--IRAC}2$ and $M_{\text{WISE}2}$ versus $\text{WISE}1\text{--WISE}2$ diagrams, the differences between the SMC and LMC are very small. This may indicate that CO absorption around $4.6 \mu\text{m}$ is much less affected by the metallicity. Finally, for the longer wavelengths (e.g., $\text{IRAC}4$, $\text{WISE}12$, and $\text{MIPS}24$ bands) where the dust emission dominates, the differences are more obvious. The LMC sample contains more dusty targets (e.g., < -10.0 mag as shown by the horizontal dotted lines) than the SMC ($N_{\text{IRAC}4\text{SMC}}/N_{\text{IRAC}4\text{LMC}} \approx 0.30$, $N_{\text{WISE}3\text{SMC}}/N_{\text{WISE}3\text{LMC}} \approx 0.35$ and $N_{\text{MIPS}24\text{SMC}}/N_{\text{MIPS}24\text{LMC}} \approx 0.38$), even though the LMC sample is more incomplete. This is likely indicating a positive relation between MLR and metallicity ([van Loon et al. 2005](#); [Mauron & Josselin 2011](#)).

Figure 11 shows multiple CCDs. Similar to the CMDs, the LMC sample always shows redder color than the SMC sample, except for the $\text{IRAC}1\text{--IRAC}2$ and $\text{WISE}1\text{--WISE}2$ colors. The differences of additional color indexes are also listed in Table 3 with corresponding limiting magnitudes.

Finally, Fig. 12 shows the median magnitude versus MAD in the WISE1 (left) and WISE2 (right) bands. In general, the difference of median values of MAD between the SMC and LMC is more significant for the brighter sources (e.g., ≤ -10.0 mag, vertical dashed line, where the bright targets start to show notable variabilities as visually inspected) as

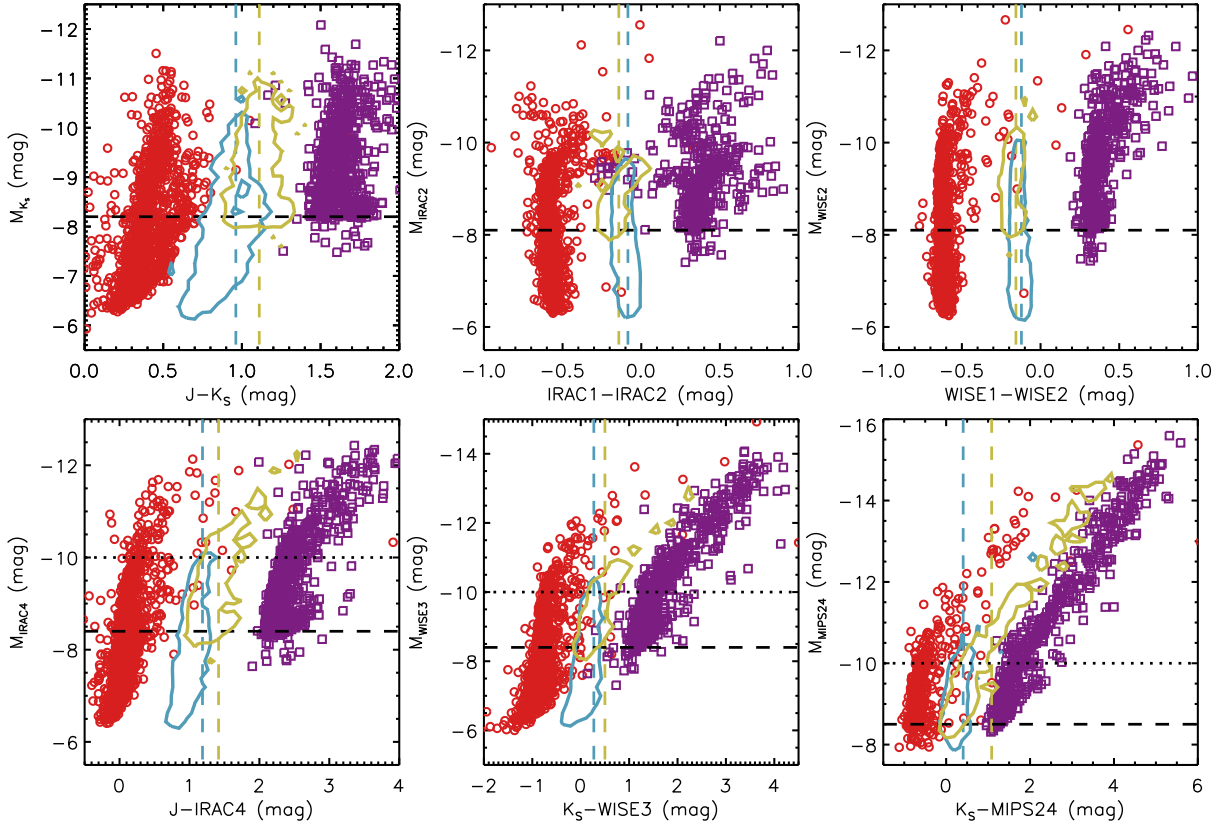


Fig. 10. CMDs of M_{K_S} vs. $J - K_S$ (upper left), $M_{\text{IRAC}2}$ vs. $\text{IRAC}1 - \text{IRAC}2$ (upper middle), $M_{\text{WISE}2}$ vs. $\text{WISE}1 - \text{WISE}2$ (upper right), $M_{\text{IRAC}4}$ vs. $J - \text{IRAC}4$ (bottom left), $M_{\text{WISE}3}$ vs. $K_S - \text{WISE}3$ (bottom middle), and $M_{\text{MIPS}24}$ vs. $K_S - \text{MIPS}24$ (bottom right). Targets with upper limits are not shown in the diagrams (same below). Red open circles and purple open squares indicate the targets from the SMC and the LMC samples, while the blue and yellow contours indicate 10% number density of each sample (same below), respectively. There are offsets of -0.5 mag (upper row) and -1.0 mag (bottom row) for the color indexes of the SMC sample, and offsets of $+0.5$ mag and $+1.0$ mag for the LMC sample, respectively (contours are not offset; same below). The vertical dashed lines indicate the median values of each color index (blue for the SMC and yellow for the LMC) with the same limiting magnitudes in both the SMC and the LMC (horizontal dashed lines). The LMC sample is not magnitude-completed and lack of a large number of fainter and bluer targets. The differences of color indexes between the SMC and the LMC are listed in Table 3. Even though the LMC sample is less complete, it still contains more dusty targets (< -10.0 mag; horizontal dotted lines) than the SMC sample at the longer wavelengths.

Table 3. Differences of color indexes between the SMC and the LMC samples.

Limiting magnitude	$\Delta(\text{SMC} - \text{LMC})$
$M_H = -8.0$ mag	$\Delta(J - H) \approx -0.059$ mag
$M_H = -8.0$ mag	$\Delta(H - K_S) \approx -0.081$ mag
$M_{K_S} = -8.2$ mag	$\Delta(J - K_S) \approx -0.15$ mag
$M_{K_S} = -8.2$ mag	$\Delta(K_S - \text{IRAC}4) \approx -0.067$ mag
$M_{\text{WISE}1} = -8.3$ mag	$\Delta(J - \text{WISE}1) \approx -0.16$ mag
$M_{\text{IRAC}2} = -8.1$ mag	$\Delta(\text{IRAC}1 - \text{IRAC}2) \approx 0.058$ mag
$M_{\text{IRAC}2} = -8.1$ mag	$\Delta(\text{IRAC}2 - \text{IRAC}3) \approx -0.055$ mag
$M_{\text{WISE}2} = -8.1$ mag	$\Delta(\text{WISE}1 - \text{WISE}2) \approx 0.035$ mag
$M_{\text{WISE}2} = -8.1$ mag	$\Delta(\text{WISE}2 - \text{WISE}3) \approx -0.022$ mag
$M_{\text{IRAC}4} = -8.4$ mag	$\Delta(J - \text{IRAC}4) \approx -0.23$ mag
$M_{\text{WISE}3} = -8.4$ mag	$\Delta(K_S - \text{WISE}3) \approx -0.23$ mag
$M_{\text{MIPS}24} = -8.5$ mag	$\Delta(K_S - \text{MIPS}24) \approx -0.68$ mag

$\text{MAD}_{\text{SMC}} - \text{MAD}_{\text{LMC}} \approx -0.0050$ mag, than the fainter sources (e.g., > -10.0 mag) as $\text{MAD}_{\text{SMC}} - \text{MAD}_{\text{LMC}} \approx -0.0012$ mag for the WISE1 band, while the difference between the whole samples is ~ -0.0045 mag, indicating that the variability of RSGs is also likely to be metallicity-dependent. Meanwhile, the differences of the WISE2 band are smaller as ~ 0.0012 mag (brighter

sources), ~ -0.0008 mag (fainter sources), and ~ -0.0035 mag (all sources), respectively, due to the lower sensitivity and larger scattering in the WISE2 band and the greater distance of the SMC.

5. Summary

We present the most comprehensive RSG sample in the SMC to date. The sample is mainly built based on a source catalog for the SMC (Yang et al. 2019) with conservative ranking (targets were identified as RSGs in at least two CMDs). Moreover, we used additional optical and MIR spectroscopic RSGs retrieved from Simbad and data taken by *Spitzer*/IRS, as well as RSG candidates selected based on the visual inspection of both *Gaia* and 2MASS CMDs. In total, the final sample contains 1239 RSG candidates with 327 unique spectroscopic RSGs. We estimate that there are ~ 1800 or more RSGs in the SMC.

We have studied the NIR to MIR properties of the RSG sample. The investigation of 2MASS CMD indicates that, at the bright magnitude end, the spectroscopic RSGs only represent about one-fourth of the whole RSG population, but follow almost exactly the MIST tracks at the red end. It also shows that many O-AGBs defined by the theoretical color cuts but located inside the MIST model region (47 out of 206 targets;

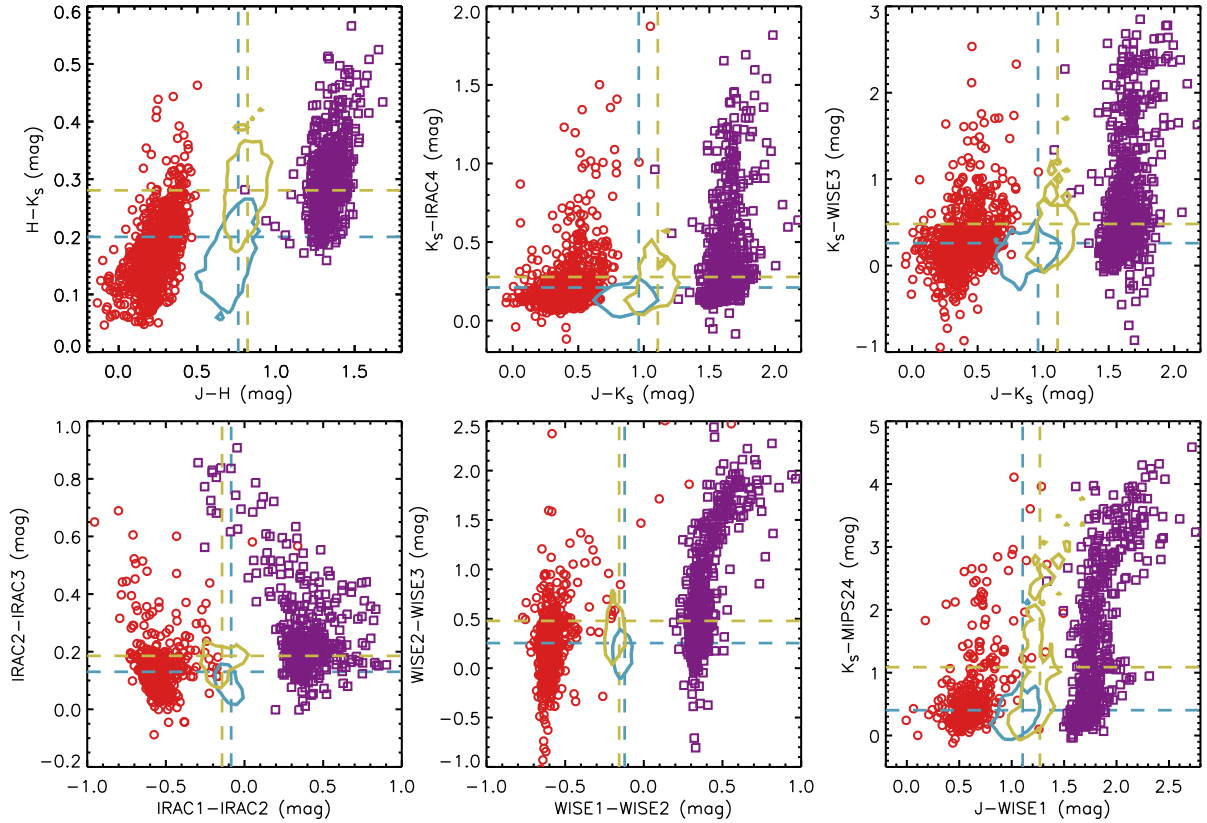


Fig. 11. CCDs of $J - H$ vs. $H - K_S$ (upper left), $J - K_S$ vs. $K_S - \text{IRAC4}$ (upper middle), $J - K_S$ vs. $K_S - \text{WISE3}$ (upper right), $\text{IRAC1} - \text{IRAC2}$ vs. $\text{IRAC2} - \text{IRAC3}$ (bottom left), $\text{WISE1} - \text{WISE2}$ vs. $\text{WISE2} - \text{WISE3}$ (bottom middle), and $J - \text{WISE1}$ vs. $K_S - \text{MIPS24}$ (bottom right). The differences of additional color indexes are also listed in Table 3.

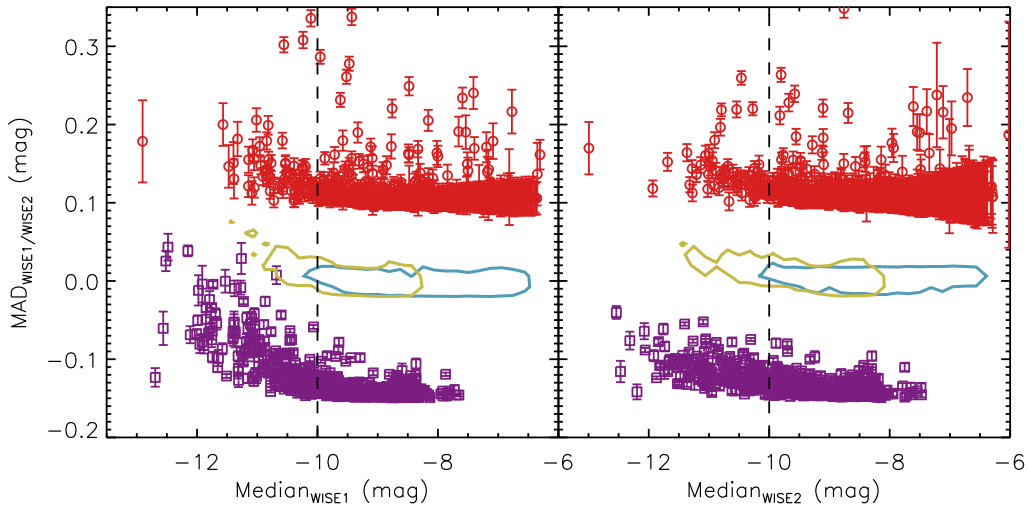


Fig. 12. Median magnitude vs. MAD in the WISE1 (left) and WISE2 (right) bands. For the WISE1 band, the differences of median values of MAD between the SMC and LMC are about -0.0050 (brighter sources; ≤ -10.0 mag shown as the vertical dashed line), -0.0012 mag (fainter sources; > -10.0 mag), and -0.0045 mag (all sources). For WISE2 band, the differences are about 0.0012 (brighter sources), -0.0008 (fainter sources), and -0.0035 mag (all sources), respectively.

$\sim 23\%$) are identified as spectroscopic RSGs by previous studies, as well as 24 C-OSARGs, 7 O-SRVs, and 3 O-Miras defined by OGLE. However, since there is a continuum with similarity and overlapping between RSGs and AGBs in both spectra and LCs, the clear separation between them is still a pending issue. Two targets that are fainter than both the K_S -TRGB and IRAC1 -TRGB are excluded from the RSG sample. We also identify one heavily obscured target by adopting $K_S > 12.7$ mag

or $\text{IRAC1} > 12.6$ mag, $J - \text{IRAC4} \geq 3.0$ mag, and $\text{IRAC4} < 10.0$ mag, based on the fact that obscured objects will be brighter and redder at the longer wavelengths compared to the shorter wavelengths.

Further analysis of CMDs with longer wavelengths indicates the complex behavior of RSG sample around $3-4\mu\text{m}$, the growth of MLR and circumstellar envelope with increasing luminosity, and a similar high MLR between RSGs and

x-AGBs for the brightest RSG candidates. The inconsistency between infrared excesses of the relatively shorter ($8\mu\text{m}$) and longer (12 and $22\mu\text{m}$) wavelengths suggests that $8\mu\text{m}$ may not be enough to characterize the MLR of brightest RSGs. The investigation of CCDs shows that there are much fewer RSGs candidates (only about 4%) showing PAH emission features compared to the Milky Way and LMC ($\sim 15\%$), which may be due to strong metallicity dependence of PAH abundance. We analyze the MIR time series data from WISE for our RSG sample. The MIR variability of the RSG sample is found to increase with luminosity, while about 21% of targets show reliable variability ($\text{MAD}_{\text{WISE1}} > 0.01$ mag). We separate the RSG sample into two subsamples (risky and safe) and identify one M5e AGB star in the risky subsample, based on the variabilities, luminosities and colors at the same time.

For the final RSG sample the degeneracy of MLR, variability, and luminosity is presented. We found that most of the high-variability targets are also the bright ones with high MLR. Although there is a linear relation between MIPS24 magnitude and MLR for the RSG sample, the fluxes of some targets is above the upper limit of 3σ of the linear relation, which may be related to the episodic mass loss events during the RSGs phase. We also roughly estimate the total dust budget produced by the entire RSG population as $\sim 1.9^{+2.4}_{-1.1} \times 10^{-6} M_{\odot} \text{yr}^{-1}$ in the most conservative case, based on the derived MLR from IRAC1–IRAC4 color, which is comparable with previous works and will be further investigated in a future paper.

Based on the MIST evolutionary tracks and synthetic photometry, we derive a linear relation between T_{eff} and observed $J - K_S$ color with reddening correction for the RSG sample. By using a constant bolometric correction and this relation, the Geneva evolutionary model is compared with our RSG sample, showing that there is a lower initial mass limit of $\sim 7 M_{\odot}$ for the RSG population as found in Yang et al. (2019). Moreover, the vast majority of targets are following the tracks, and few outliers can be explained by the combination of variability and reddening as mentioned in Yang et al. (2018).

Finally, we compare the RSG sample in the LMC (Yang et al. 2018) and the final RSG sample in the SMC. Despite the incompleteness of LMC sample in the faint end, the result indicates that the LMC sample is always redder than the SMC sample, except for the IRAC1–IRAC2 and WISE1–WISE2 colors (indicating CO absorption around $4.6\mu\text{m}$ may be much less affected by the metallicity). The difference is more obvious at the longer wavelengths, which likely indicates a positive relation between MLR and metallicity. Moreover, a similar result is found for the MIR variability, as the LMC sample shows higher variability than the SMC sample, and it is more significant for the brighter sources than the fainter sources, which indicates that the variability of RSGs also likely to be metallicity dependent.

We are currently in the process of investigating the evolved massive star populations (including a much more complete sample of RSGs) in the LMC. We also plan to further explore the RSG population in the nearby low-metallicity dwarf galaxies, by utilizing deep optical, NIR, and MIR photometric data. Our studies will help provide a more comprehensive view of evolution and dust production of evolved massive stars at low-metallicity environment.

Acknowledgements. We would like to thank the anonymous referee for many constructive comments and suggestions. This study has received funding from the European Research Council (ERC) under the European Union’s Horizon 2020 research and innovation programme (grant agreement number 772086). B.W.J. and J.G. gratefully acknowledge support from the National Natural Science Foundation of China (Grant No.11533002 and U1631104). We thank M.

A. T. Groenewegen and G. C. Sloan help on the calculation of MLR. We thank Man I Lam and Stephen A. S. de Wit for helpful comments and suggestions. This publication makes use of data products from the Two Micron All Sky Survey, which is a joint project of the University of Massachusetts and the Infrared Processing and Analysis Center/California Institute of Technology, funded by the National Aeronautics and Space Administration and the National Science Foundation. This work is based in part on observations made with the *Spitzer* Space Telescope, which is operated by the Jet Propulsion Laboratory, California Institute of Technology under a contract with NASA. This publication makes use of data products from the Wide-field Infrared Survey Explorer, which is a joint project of the University of California, Los Angeles, and the Jet Propulsion Laboratory/California Institute of Technology. It is funded by the National Aeronautics and Space Administration. This publication makes use of data products from the Near-Earth Object Wide-field Infrared Survey Explorer (NEOWISE), which is a project of the Jet Propulsion Laboratory/California Institute of Technology. NEOWISE is funded by the National Aeronautics and Space Administration. This research has made use of the NASA/IPAC Infrared Science Archive, which is operated by the Jet Propulsion Laboratory, California Institute of Technology, under contract with the National Aeronautics and Space Administration. This work has made use of data from the European Space Agency (ESA) mission *Gaia* (<https://www.cosmos.esa.int/gaia>), processed by the *Gaia* Data Processing and Analysis Consortium (DPAC, <https://www.cosmos.esa.int/web/gaia/dpac/consortium>). Funding for the DPAC has been provided by national institutions, in particular the institutions participating in the *Gaia* Multilateral Agreement. This research has made use of the SIMBAD database and VizieR catalog access tool, operated at CDS, Strasbourg, France, and the Tool for OPERations on Catalogues And Tables (TOPCAT; Taylor 2005).

References

- Barba, R. H., Niemela, V. S., Baume, G., & Vazquez, R. A. 1995, *ApJ*, 446, L23
 Beasor, E. R., & Davies, B. 2016, *MNRAS*, 463, 1269
 Bessell, M. S., Brett, J. M., Scholz, M., & Wood, P. R. 1991, *A&AS*, 89, 335
 Bessell, M. S., Scholz, M., & Wood, P. R. 1996, *A&A*, 307, 481
 Bonanos, A. Z., Massa, D. L., Sewilo, M., et al. 2009, *AJ*, 138, 1003
 Bonanos, A. Z., Lennon, D. J., Köhlinger, F., et al. 2010, *AJ*, 140, 416
 Britavskiy, N. E., Bonanos, A. Z., Mehner, A., et al. 2015, *A&A*, 584, A33
 Britavskiy, N., Lennon, D. J., Patrick, L. R., et al. 2019, *A&A*, 624, A128
 Bouret, J.-C., Lanz, T., Martins, F., et al. 2013, *A&A*, 555, A1
 Boyer, M. L., Srinivasan, S., van Loon, J. T., et al. 2011, *AJ*, 142, 103
 Boyer, M. L., Srinivasan, S., Riebel, D., et al. 2012, *ApJ*, 748, 40
 Buchanan, C. L., Kastner, J. H., Forrest, W. J., et al. 2006, *AJ*, 132, 1890
 Castro, N., Oey, M. S., Fossati, L., & Langer, N. 2018, *ApJ*, 868, 57
 Chen, R., Luo, A., Liu, J., et al. 2016, *AJ*, 151, 146
 Cioni, M.-R. L., van der Marel, R. P., Loup, C., & Habing, H. J. 2000, *A&A*, 359, 601
 Cioni, M.-R. L., Girardi, L., Marigo, P., & Habing, H. J. 2006a, *A&A*, 448, 77
 Cioni, M.-R. L., Girardi, L., Marigo, P., & Habing, H. J. 2006b, *A&A*, 452, 195
 Chatys, F. W., Bedding, T. R., Murphy, S. J., et al. 2019, *MNRAS*, 487, 4832
 Chiosi, C., & Maeder, A. 1986, *ARA&A*, 24, 329
 Choi, J., Dotter, A., Conroy, C., et al. 2016, *ApJ*, 823, 102
 Cirasuolo, M., Afonso, J., Bender, R., et al. 2012, *Proc. SPIE*, 8446, 84460S
 de Jong, R. S., Bellido-Tirado, O., Chiappini, C., et al. 2012, *Proc. SPIE*, 8446, 84460T
 Davies, B., & Beasor, E. R. 2018, *MNRAS*, 474, 2116
 Davies, B., Kudritzki, R.-P., & Figer, D. F. 2010, *MNRAS*, 407, 1203
 Davies, B., Kudritzki, R.-P., Plez, B., et al. 2013, *ApJ*, 767, 3
 Davies, B., Kudritzki, R.-P., Lardo, C., et al. 2017, *ApJ*, 847, 112
 Dobbie, P. D., Cole, A. A., Subramaniam, A., & Keller, S. 2014, *MNRAS*, 442, 1680
 Doherty, C. L., Gil-Pons, P., Siess, L., et al. 2017, *PASA*, 34, e056
 D’Onghia, E., & Fox, A. J. 2016, *ARA&A*, 54, 363
 Dorda, R., Negueruela, I., González-Fernández, C., & Tabernero, H. M. 2016, *A&A*, 592, A16
 Dorda, R., Negueruela, I., González-Fernández, C., & Marco, A. 2018, *A&A*, 618, A137
 Dotter, A. 2016, *ApJS*, 222, 8
 Draine, B. T., Dale, D. A., Bendo, G., et al. 2007, *ApJ*, 663, 866
 Elias, J. H., & Frogel, J. A. 1985, *ApJ*, 289, 141
 Ekström, S., Georgy, C., Eggenberger, P., et al. 2012, *A&A*, 537, A146
 Ekström, S., Georgy, C., Meynet, G., Groh, J., & Granada, A. 2013, *EAS Pub. Ser.*, 60, 31
 Engelbracht, C. W., Gordon, K. D., Rieke, G. H., et al. 2005, *ApJ*, 628, L29
 Evans, C. J., & Howarth, I. D. 2008, *MNRAS*, 386, 826
 Feast, M. W., Catchpole, R. M., Carter, B. S., & Roberts, G. 1980, *MNRAS*, 193, 377
 Gaia Collaboration (Prusti, T., et al.) 2016, *A&A*, 595, A1

- Gaia Collaboration (Brown, A. G. A., et al.) 2018, *A&A*, 616, A1
- Gao, J., Jiang, B. W., Li, A., & Xue, M. Y. 2013, *ApJ*, 776, 7
- Georgy, C., Ekström, S., Eggenberger, P., et al. 2013, *A&A*, 558, A103
- González-Fernández, C., Dorda, R., Negueruela, I., & Marco, A. 2015, *A&A*, 578, A3
- Graczyk, D., Pietrzyński, G., Thompson, I. B., et al. 2014, *ApJ*, 780, 59
- Groenewegen, M. A. T., & Sloan, G. C. 2018, *A&A*, 609, A114
- Groenewegen, M. A. T., Sloan, G. C., Soszyński, I., & Petersen, E. A. 2009, *A&A*, 506, 1277
- Hainich, R., Pasemann, D., Todt, H., et al. 2015, *A&A*, 581, A21
- Harper, G. M., Brown, A., & Lim, J. 2001, *ApJ*, 551, 1073
- Herwig, F. 2005, *ARA&A*, 43, 435
- Höfner, S., & Olofsson, H. 2018, *A&ARv*, 26, 1
- Houck, J. R., Roellig, T. L., van Cleve, J., et al. 2004, *ApJS*, 154, 18
- Humphreys, R. M. 2010, *Hot and Cool: Bridging Gaps in Massive Star Evolution* (San Francisco: ASP), 425, 247
- Humphreys, R. M., & Davidson, K. 1979, *ApJ*, 232, 409
- Jacyszyn-Dobrzyniecka, A. M., Skowron, D. M., Mróz, P., et al. 2016, *Acta Astron.*, 66, 149
- Josselin, E., & Plez, B. 2007, *A&A*, 469, 671
- Josselin, E., Blommaert, J. A. D. L., Groenewegen, M. A. T., Omont, A., & Li, F. L. 2000, *A&A*, 357, 225
- Justtanont, K., & Tielens, A. G. G. M. 1992, *ApJ*, 389, 400
- Keller, S. C., & Wood, P. R. 2006, *ApJ*, 642, 834
- Kemper, F., Sylvester, R. J., Barlow, M. J., et al. 2000, *Thermal Emission Spectroscopy and Analysis of Dust, Disks, and Regoliths*, 15
- Kiss, L. L., Szabó, G. M., & Bedding, T. R. 2006, *MNRAS*, 372, 1721
- Kourmliotis, M., Bonanos, A. Z., Soszyński, I., et al. 2014, *A&A*, 562, A125
- Kraemer, K. E., Sloan, G. C., Wood, P. R., Jones, O. C., & Egan, M. P. 2017, *ApJ*, 834, 185
- Levesque, E. M. 2010, *New Astron. Rev.*, 54, 1
- Levesque, E. M. 2013, *EAS Pub. Ser.*, 60, 269
- Levesque, E. M., & Massey, P. 2012, *AJ*, 144, 2
- Levesque, E. M., Massey, P., Olsen, K. A. G., et al. 2005, *ApJ*, 628, 973
- Levesque, E. M., Massey, P., Olsen, K. A. G., et al. 2006, *ApJ*, 645, 1102
- MacGregor, K. B., & Stencel, R. E. 1992, *ApJ*, 397, 644
- Marshall, J. R., van Loon, J. T., Matsuura, M., et al. 2004, *MNRAS*, 355, 1348
- Massey, P. 2013, *New Astron. Rev.*, 57, 14
- Massey, P., & Olsen, K. A. G. 2003, *AJ*, 126, 2867
- Massey, P., Plez, B., Levesque, E. M., et al. 2005, *ApJ*, 634, 1286
- Massey, P., Levesque, E. M., Olsen, K. A. G., Plez, B., & Skiff, B. A. 2007, *ApJ*, 660, 301
- Matsuura, M., Woods, P. M., & Owen, P. J. 2013, *MNRAS*, 429, 2527
- Mauron, N., & Josselin, E. 2011, *A&A*, 526, A156
- Messineo, M., Menten, K. M., Churchwell, E., & Habing, H. 2012, *A&A*, 537, A10
- Meynet, G., Chomienne, V., Ekström, S., et al. 2015, *A&A*, 575, A60
- Muraveva, T., Subramanian, S., Clementini, G., et al. 2018, *MNRAS*, 473, 3131
- Neugent, K. F., Massey, P., Skiff, B., et al. 2010, *ApJ*, 719, 1784
- Neugent, K. F., Massey, P., Skiff, B., & Meynet, G. 2012, *ApJ*, 749, 177
- O'Halloran, B., Satyapal, S., & Dudik, R. P. 2006, *ApJ*, 641, 795
- Pawlak, M., Soszyński, I., Udalski, A., et al. 2016, *Acta Astron.*, 66, 421
- Paxton, B., Bildsten, L., Dotter, A., et al. 2011, *ApJS*, 192, 3
- Paxton, B., Cantiello, M., Arras, P., et al. 2013, *ApJS*, 208, 4
- Paxton, B., Marchant, P., Schwab, J., et al. 2015, *ApJS*, 220, 15
- Paxton, B., Schwab, J., Bauer, E. B., et al. 2018, *ApJS*, 234, 34
- Pietrzyński, G., Graczyk, D., Gieren, W., et al. 2013, *Nature*, 495, 76
- Rayner, J. T., Cushing, M. C., & Vacca, W. D. 2009, *ApJS*, 185, 289
- Ren, Y., Jiang, B.-W., Yang, M., & Gao, J. 2019, *ApJS*, 241, 35
- Reiter, M., Marengo, M., Hora, J. L., & Fazio, G. G. 2015, *MNRAS*, 447, 3909
- Rieke, G. H., & Lebofsky, M. J. 1985, *ApJ*, 288, 618
- Rolleston, W. R. J., Trundle, C., & Dufton, P. L. 2002, *A&A*, 396, 53
- Rousseuw, P. J., & Croux, C. 1993, *J. Am. Stat. Assoc.*, 88, 1273
- Ruffle, P. M. E., Kemper, F., Jones, O. C., et al. 2015, *MNRAS*, 451, 3504
- Russell, S. C., & Dopita, M. A. 1992, *ApJ*, 384, 508
- Scowcroft, V., Freedman, W. L., Madore, B. F., et al. 2016, *ApJ*, 816, 49
- Seok, J. Y., Hirashita, H., & Asano, R. S. 2014, *MNRAS*, 439, 2186
- Shivaei, I., Reddy, N. A., Shapley, A. E., et al. 2017, *ApJ*, 837, 157
- Siess, L. 2006, *A&A*, 448, 717
- Skrutskie, M. F., Cutri, R. M., Stiening, R., et al. 2006, *AJ*, 131, 1163
- Sloan, G. C., Kraemer, K. E., Wood, P. R., et al. 2008, *ApJ*, 686, 1056
- Smartt, S. J., Eldridge, J. J., Crockett, R. M., & Maund, J. R. 2009, *MNRAS*, 395, 1409
- Smith, N. 2014, *ARA&A*, 52, 487
- Smith, N., Hinkle, K. H., & Ryde, N. 2009, *AJ*, 137, 3558
- Soraisam, M. D., Bildsten, L., Drout, M. R., et al. 2018, *ApJ*, 859, 73
- Soszyński, I., Udalski, A., Szymański, M. K., et al. 2009, *Acta Astron.*, 59, 239
- Soszyński, I., Udalski, A., Szymański, M. K., et al. 2011, *Acta Astron.*, 61, 217
- Soszyński, I., Udalski, A., Szymański, M. K., et al. 2015, *Acta Astron.*, 65, 297
- Soszyński, I., Udalski, A., Szymański, M. K., et al. 2018, *Acta Astron.*, 68, 89
- Srinivasan, S., Boyer, M. L., Kemper, F., et al. 2016, *MNRAS*, 457, 2814
- Sylvester, R. J., Kemper, F., Barlow, M. J., et al. 1999, *A&A*, 352, 587
- Szymanski, M. K. 2005, *Acta Astron.*, 55, 43
- Taberner, H. M., Dorda, R., Negueruela, I., et al. 2018, *MNRAS*, 476, 3106
- Taylor, M. B. 2005, *Astronomical Data Analysis Software and Systems XIV* (San Francisco: Astronomical Society of the Pacific), 347, 29
- Udalski, A., Szymanski, M., Kaluzny, J., Kubiak, M., & Mateo, M. 1992, *Acta Astron.*, 42, 253
- Udalski, A., Szymanski, M. K., Soszynski, I., & Poleski, R. 2008, *Acta Astron.*, 58, 69
- Udalski, A., Szymański, M. K., & Szymański, G. 2015, *Acta Astron.*, 65, 1
- van Loon, J. T., Groenewegen, M. A. T., de Koter, A., et al. 1999, *A&A*, 351, 559
- van Loon, J. T., Cioni, M.-R. L., Zijlstra, A. A., & Loup, C. 2005, *A&A*, 438, 273
- van Loon, J. T., Marshall, J. R., Cohen, M., et al. 2006, *A&A*, 447, 971
- van Loon, J. T., Cohen, M., Oliveira, J. M., et al. 2008, *A&A*, 487, 1055
- Verhoelst, T., van der Zypen, N., Hony, S., et al. 2009, *A&A*, 498, 127
- Wachter, S., Mauerhan, J. C., Van Dyk, S. D., et al. 2010, *AJ*, 139, 2330
- Wang, S., & Chen, X. 2019, *ApJ*, 877, 116
- Wenger, M., Ochsenbein, F., Egret, D., et al. 2000, *A&AS*, 143, 9
- Werner, M. W., Roellig, T. L., Low, F. J., et al. 2004, *ApJS*, 154, 1
- Whitelock, P. A., Feast, M. W., Menzies, J. W., et al. 1989, *MNRAS*, 238, 769
- Wood, P. R., Bessell, M. S., & Fox, M. W. 1983, *ApJ*, 272, 99
- Wright, E. L., Eisenhardt, P. R. M., Mainzer, A. K., et al. 2010, *AJ*, 140, 1868
- Yang, M. 2019, *A Synoptic View of the Magellanic Clouds: VMC, Gaia and Beyond*, 17
- Yang, M., & Jiang, B. W. 2011, *ApJ*, 727, 53
- Yang, M., & Jiang, B. W. 2012, *ApJ*, 754, 35
- Yang, M., Bonanos, A. Z., Jiang, B.-W., et al. 2018, *A&A*, 616, A175
- Yang, M., Bonanos, A. Z., Jiang, B.-W., et al. 2019, *A&A*, 629, A91
- Yoon, S.-C., & Cantiello, M. 2010, *ApJ*, 717, L62